Copy

NASA Project Apollo Working Paper No. 1021

PROJECT APOLLO

INVESTIGATION OF NEWTONIAN STATIC LONGITUDINAL AERODYNAMIC CHARACTERISTICS OF BODIES OF REVOLUTION WITH VARIOUS HEAT-SHIELD CURVATURES, AFTERBODY ANGLES, AND CORNER-EDGE RADII

NATIONAL AERONAUTICS AND SPACE ADMINISTRATION

SPACE TASK GROUP

Langley Field, Va.

June 28, 1961

NASA PROJECT APOLLO WORKING PAPER NO. 1021

PROJECT APOLLO

INVESTIGATION OF NEWTONIAN STATIC LONGITUDINAL AERODYNAMIC CHARACTERISTICS OF BODIES OF REVOLUTION WITH VARIOUS HEAT-SHIELD CURVATURES, AFTERBODY ANGLES, AND CORNER-EDGE RADII

Prepared by: Edward E. Mayo

Edward E. Mayo
AST, Flight Mechanics

Thomas L. Blakemore

Thomas L. Blakemore
AST, Flight Mechanics

Authorized for Distribution:

Robert R. Gilruth, Director

NATIONAL AERONAUTICS AND SPACE ADMINISTRATION

SPACE TASK GROUP

Langley Field, Va.

June 28, 1961

TABLE OF CONTENTS

LIST OF FIGURES

INVESTIGATION OF NEWTONIAN STATIC LONGITUDINAL AERODYNAMIC CHARACTERISTICS OF BODIES OF REVOLUTION WITH VARIOUS HEAT-SHIELD CURVATURES, AFTERBODY ANGLES, AND CORNER-EDGE RADII

SUMMARY

Newtonian aerodynamic coefficients are presented for preliminary prediction of the static stability characteristics of bluff reentry bodies with various heat-shield curvatures, afterbody angles, and corner-edge radii. An example of the usefulness of these design curves is presented in the appendix where the aerodynamics characteristics are computed for several configurations of equal volume.

INTRODUCTION

The purpose of this paper is to present Newtonian aerodynamic coefficients for preliminary prediction of the hypersonic static stability characteristics of bluff reentry capsules with various heat-shield curvatures, afterbody cone angles, and corner-edge radii. As an example of the usefulness of the design curves, the static stability characteristics of several configurations of equal volumes are calculated and compared.

PROCEDURE AND ACCURACIES

This paper consists basically of two separate investigations: heat-shield curvature and afterbody-angle investigation, and corner-edge radius investigation. All aerodynamic coefficients presented, except the afterbody contribution, were determined by numerically integrating the Newtonian pressure coefficients on an IBM 704 digital computer, utilizing a program set up for bodies of revolution. The afterbody contribution was computed from algebraic Newtonian aerodynamic coefficient functions. All coefficients were computed for every ten-degrees angle-of-attack and would correspond to a maximum stagnation point pressure coefficient of 2, $(M = \infty, \gamma = 1)$. Some idea of the accuracy of the numerical integration procedure may be obtained by comparing the integrated values for the sphere $\left(R_C/D = 0.50, \text{fig. } 4\right)$, with exact values. For the sphere at any

angle of attack, the exact Newtonian value of the lift coefficient is zero and the drag coefficient 1. The maximum deviation of the integrated values of the lift and the drag coefficients from these exact values is 0.005 and 0.013, respectively.

SYMBOLS

C_A	axial-force coefficient, $\frac{\text{Axial force}}{qS}$
C_D	drag coefficient, $\frac{\text{Drag force}}{qS}$
C_L	lift coefficient, $\frac{\text{Lift force}}{qS}$
L/D	lift-to-drag ratio
C_m	pitching-moment coefficient, $\frac{\text{Pitching moment}}{qSD}$
C_{m_α}	pitching-moment-curve slope, per degree at $\alpha \approx 0^\circ$, $\frac{\partial C_m}{\partial \alpha}$
C_N	normal-force coefficient, $\frac{\text{Normal force}}{qS}$
D	configuration maximum diameter
D'	configuration diameter at station of afterbody–corner-edge junction. (See insert figure, fig. 8.)
M_∞	free-stream Mach number
q	free-stream dynamic pressure
R_C	corner-edge radius
R_N	heat-shield radius
S	configuration cross-sectional area at station of maximum diameter
x	distance from most forward point of configuration to station of maximum diameter. (See insert figure, fig. 9.)

x' distance from station of maximum diameter to station of afterbody corner-edge junction. (See insert figure, fig. 9.) $\frac{x'}{D} = \left(R_C/D\right) \sin \theta_v$

$X_{c.g.}$ distance from most forward point of configuration to center-of-gravity location along axis of symmetry

$Y_{c.g.}$ lateral distance from axis of symmetry to center-of-gravity location

α angle of attack of model centerline, deg

γ ratio of specific heats

θ_v afterbody angle, deg

DISCUSSION AND PRESENTATION OF RESULTS

The effects of heat-shield curvature and afterbody angle on the static stability characteristics are presented in figure 3 for an $X_{c.g.}$ location at the configuration maximum diameter, angle-of-attack range from 0° to 90°, heat-shield radius of curvature to diameter ratios of 0.8, 1.2, 1.6, ∞, and afterbody angles of 0°, 10°, 20°, 30°, 40°, 50° and 60°. (See fig. 1.) The heat-shield contribution and afterbody contribution to the stability characteristics are presented separately in figures 3(a) and 3(b), respectively. The heat shield and afterbody characteristics are combined in figure 3(c) and the maximum lift-to-drag ratios and maximum lift coefficients for the combined heat shield and afterbody are presented in figure 5. The values in figure 5 were read from the faired curves in figure 3. Since the coefficients presented in figure 3 were calculated in 10° increments, the conditions at maximum lift-to-drag ratios and maximum lift are not accurately defined. Therefore, the grid was dropped from figure 5. From figure 5, it is seen that an increase in maximum lift-to-drag ratio and an increase in maximum lift is obtained by decreasing the heat-shield curvature $\left(\text{increasing } R_N/D\right)$ and/or by increasing the afterbody angle. This results in a decrease in static stability as illustrated by the pitching-moment curves of figures 3(a), 3(b), and 3(c). For the heat-shield contribution shown in figure 3(a), the normal-force coefficient increases while the axial-force coefficient decreases with decreasing R_N/D $(\alpha < 55^\circ)$. Thus the orientation angle of the resultant force vector $\left(\text{angle whose tangent is } C_N/C_A\right)$ increases with decreasing R_N/D.

The effects of corner-edge radius on the static stability characteristics are presented in figure 4 and summarized in figure 6 for an $X_{c.g.}$ location of D/3, angle-of-attack range from 0° to 80°, corner-edge radius to diameter ratio from 0 to 0.5, and heat-shield radius to diameter ratios of 1.0 and 1.5. (See fig. 2.) From figures 6(a) and 6(c), it is seen that increasing corner-edge radius decreases the absolute value of L/D, whereas, decreasing the heat-shield curvature increases the absolute value of L/D. For moderate corner-edge radii $\left(R_c/D\right) \lesssim 0.2$, increasing the corner-edge radius decreases the static stability; whereas, for very large corner-edge radii $\left(R_c/D\right) \gtrsim 0.3$ increasing the corner-edge radius increases the static stability. (See fig. 6(b).) It is also seen from figure 6(b) that the flatter the heat shield, the smaller the effect of corner-edge radius on the static stability. Figure 6(b) also illustrates (again) that flattening the heat shield decreases the static stability. The orientation angle of the resultant force vector is seen from figure 4(a) to increase with increasing R_c/D.

The reference area ratio and moment reference distances for combining desired corner-edge radius and afterbody contributions are given in figures 7 and 8. An example of combining these contributions is presented in the appendix where the aerodynamic characteristics are computed for several configurations of equal volumes.

CONCLUSIONS

1. Decreasing the heat-shield curvature and/or increasing the afterbody angle increases the maximum lift-to-drag ratio and the maximum lift coefficient while decreasing the static stability.

2. Increasing corner-edge radius decreases the maximum lift-to-drag ratio. For moderate corner-edge radius, increasing corner-edge radius decreases the static stability; whereas, for very large corner-edge radius, increasing the corner-edge radius increases the static stability. Decreasing the heat-shield curvature reduces the effect of corner-edge radius on the static stability.

3. The orientation angle of the resulting reentry force vector increases with increasing heat-shield curvature and increasing corner-edge radius.

4. In comparing the aerodynamic characteristics of several capsules of equal volume with increasing corner-edge radius (resulting in increasing afterbody angle), the effects of the increased corner-edge radius were dominant, resulting in a decreased $(L/D)_{max}$ and $C_{L_{max}}$.

APPENDIX

As an example of combining the corner-edge radius and afterbody contributions presented in figures 1 through 8, the aerodynamics of a typical lunar reentry capsule are presented. The capsule was designed for a hypersonic lift-to-drag capability of 0.7.

The minimum volume requirements for the crew and equipment fixed the afterbody angle at 30°. The afterbody angle resulting from the volume requirement was based on a 13-foot diameter capsule and a semi-integrated module concept (lunar vehicle consisting of a command and an equipment module). The lift-to-drag ratio capability requirement fixed the heat-shield radius of curvature to diameter ratio at 1.2. (See fig. 5.) The center-of-gravity location has been estimated as 0.24 diameter behind the heat shield. Since corner-edge radius is desired for the configuration because of the high local convective heating rates associated with the very large velocity gradients resulting from the sharp corner, the basic configuration reentry aerodynamics are compared with two other configurations of equal volume whose corner-edge radius to diameter ratios are 0.05 and 0.10. (See fig. A-1.) The resulting afterbody angles to hold the volume constant are approximately 35° and 40°, respectively.

The aerodynamic characteristics of the configurations are presented in figure A-2 and the lateral center-of-gravity offsets required to trim the configurations at various lift-to-drag ratios are presented in figure A-3 for the longitudinal center-of-gravity location to diameter ratio of 0.24.

The forebody coefficients were obtained by interpolating from figure 4 for a heat-shield radius to diameter ratio of 1.2 and the afterbody coefficients were obtained from figure 3(b). The combined coefficients, which are presented in figure A-2, were then computed with the use of figures 7 and 8 as follows:

$$C_A,\ C_N,\ C_L,\ C_D = \left(C_A,\ C_N,\ C_L,\ C_D\right)_{\text{forebody}} + \left(\frac{D'}{D}\right)^2 \left(C_A,\ C_N,\ C_L,\ C_D\right)_{\text{afterbody}}$$

$$C_m = C_{m_{\text{forebody}}} + \left(\frac{X_{c.g.}}{D} - 0.333\right) C_{N_{\text{forebody}}} + C_{m_{\text{afterbody}}} \left(\frac{D'}{D}\right)^3$$

$$+ C_{N_{\text{afterbody}}} \left[\frac{X_{c.g.}}{D} - \left(\frac{x}{D} + \frac{x'}{D}\right)\right] \left(\frac{D'}{D}\right)^2$$

It should be emphasized that small inaccuracies occur in combining the corner-edge radius and afterbody contributions in that a small portion of the corner-edge radius is shielded by the conical afterbody. For the large afterbody angle and small corner-edge radii of the present investigation, the inaccuracies would be negligible.

The data in figure A-2 shows that a maximum lift-to-drag ratio range from -0.64 to -0.80 is attained for the configurations at approximately 50° angle of attack. The maximum lift coefficient ranges from -0.53 to -0.69 and occurs at approximately 35° angle of attack. From figure A-3, it is seen that the vehicle may be trimmed at a lift-to-drag ratio of -0.5 by lateral center-of-gravity offset. Trim from an L/D of -0.5 $\left(\text{lower side of } C_{L_{max}}\right)$ to $(L/D)_{max}$ could be accomplished by augmenting the lateral center-of-gravity offset with an auxiliary flap. The change in orientation of the resultant reentry force vector in trimming the $R_C/D = 0$, 0.05, and 0.10 vehicles from $\alpha = 0$ to $C_{L_{max}}$ is approximately 4.0°, 6.5° and 11.5° respectively and in trimming from $C_{L_{max}}$ to $(L/D)_{max}$ is approximately 13.5°, 14.5°, and 11.5°, respectively. The comparison of the configurations in figure A-2 shows that the effect of increasing the corner-edge radius was dominant over the effect of the resulting increase in afterbody angle and thus produced a decrease in $(L/D)_{max}$ and $C_{L_{max}}$.

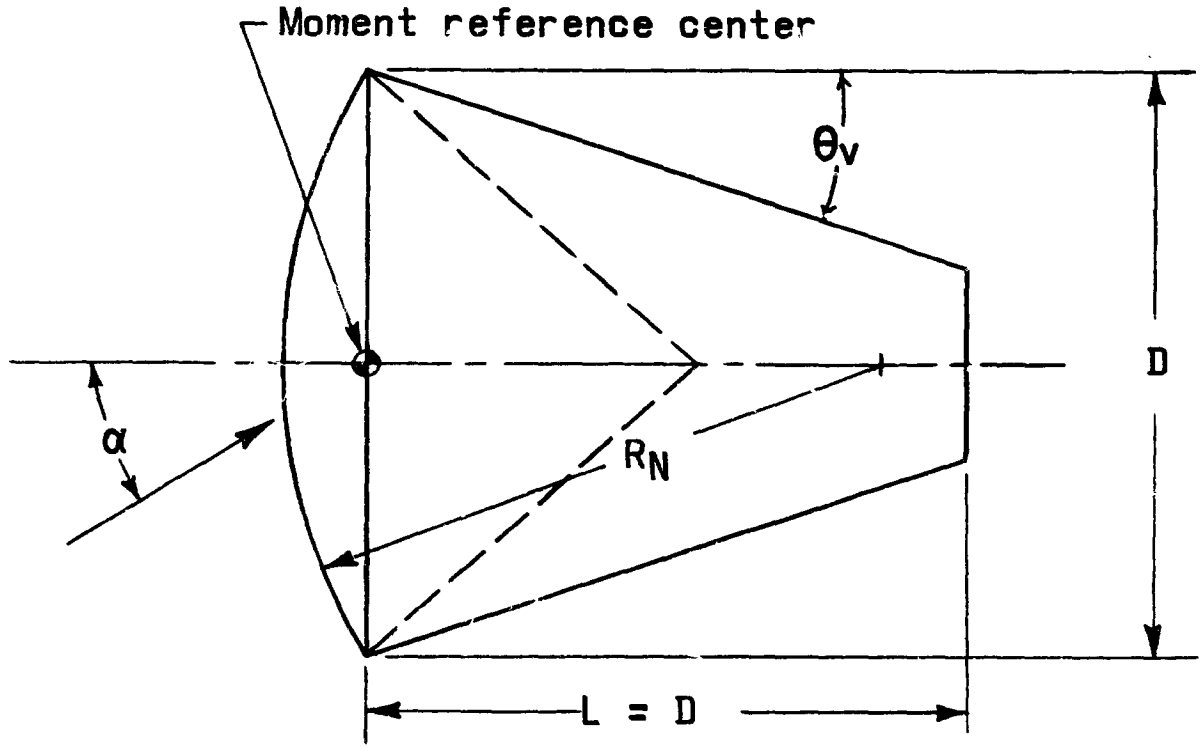

Range of variables:

α = 0 to 90 deg

$\frac{R_N}{D}$ = 0.8, 1.2, 1.6, ∞

θ_V = 0, 10, 20, 30, 40, 50, 60 deg

Figure 1.- Configuration for heat-shield curvature and afterbody angle investigation.

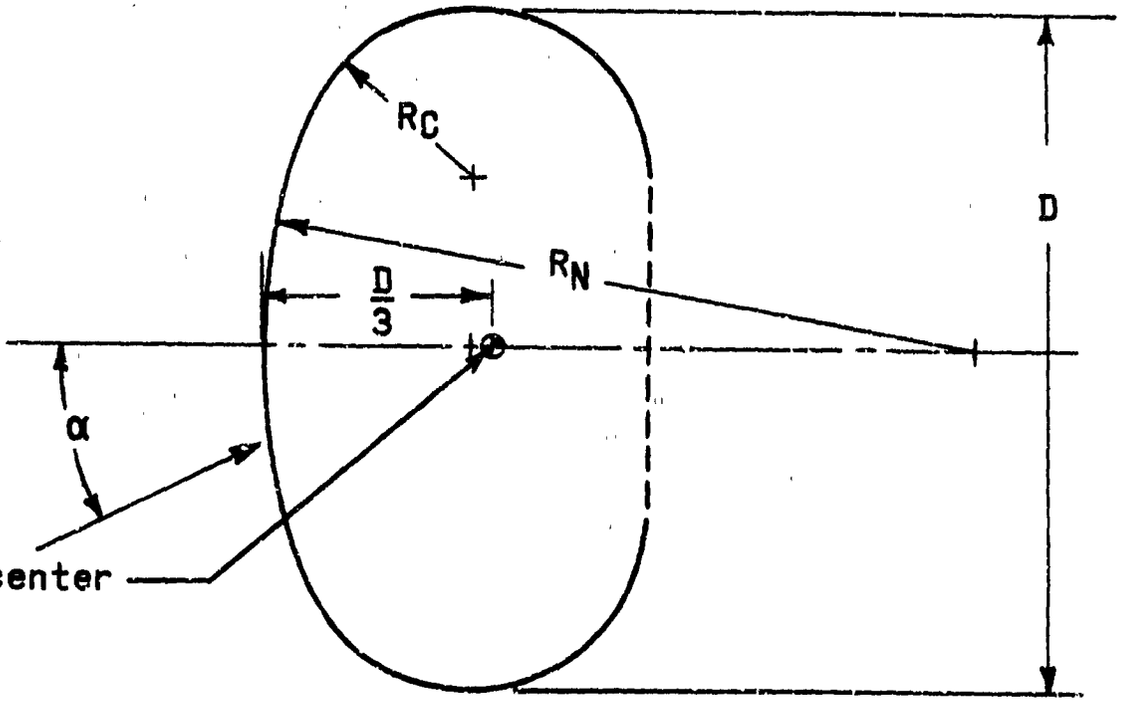

Range of variables:

α = 0 to 80 deg

$\frac{R_C}{D}$ = 0, .05, .10, .15, .20, .25, .50

$\frac{R_N}{D}$ = 1.0, 1.5

Figure 2.- Configuration for corner-edge radius investigation.

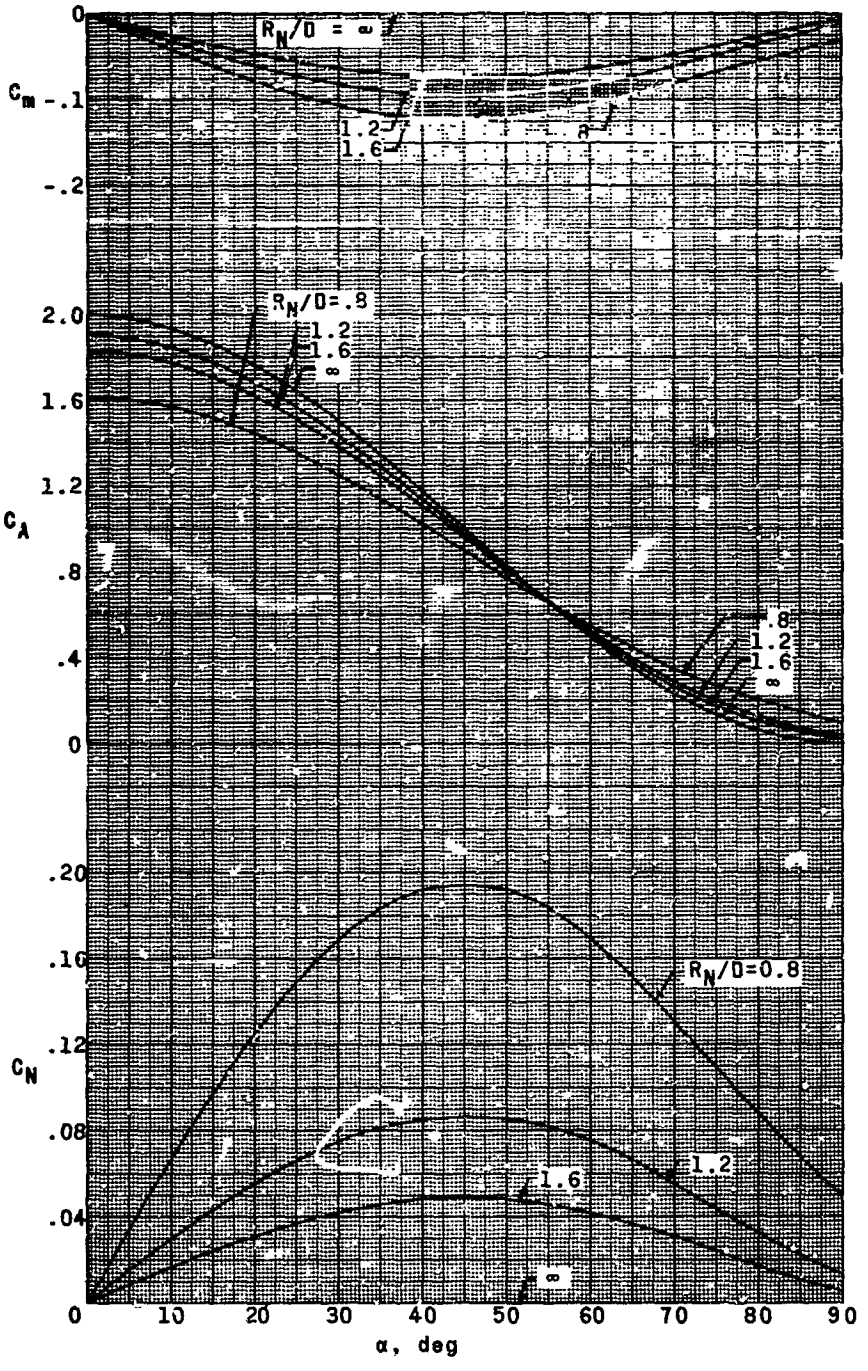

(a) Heat-shield contribution.

Figure 3.- Heat-shield curvature and afterbody angle investigation.

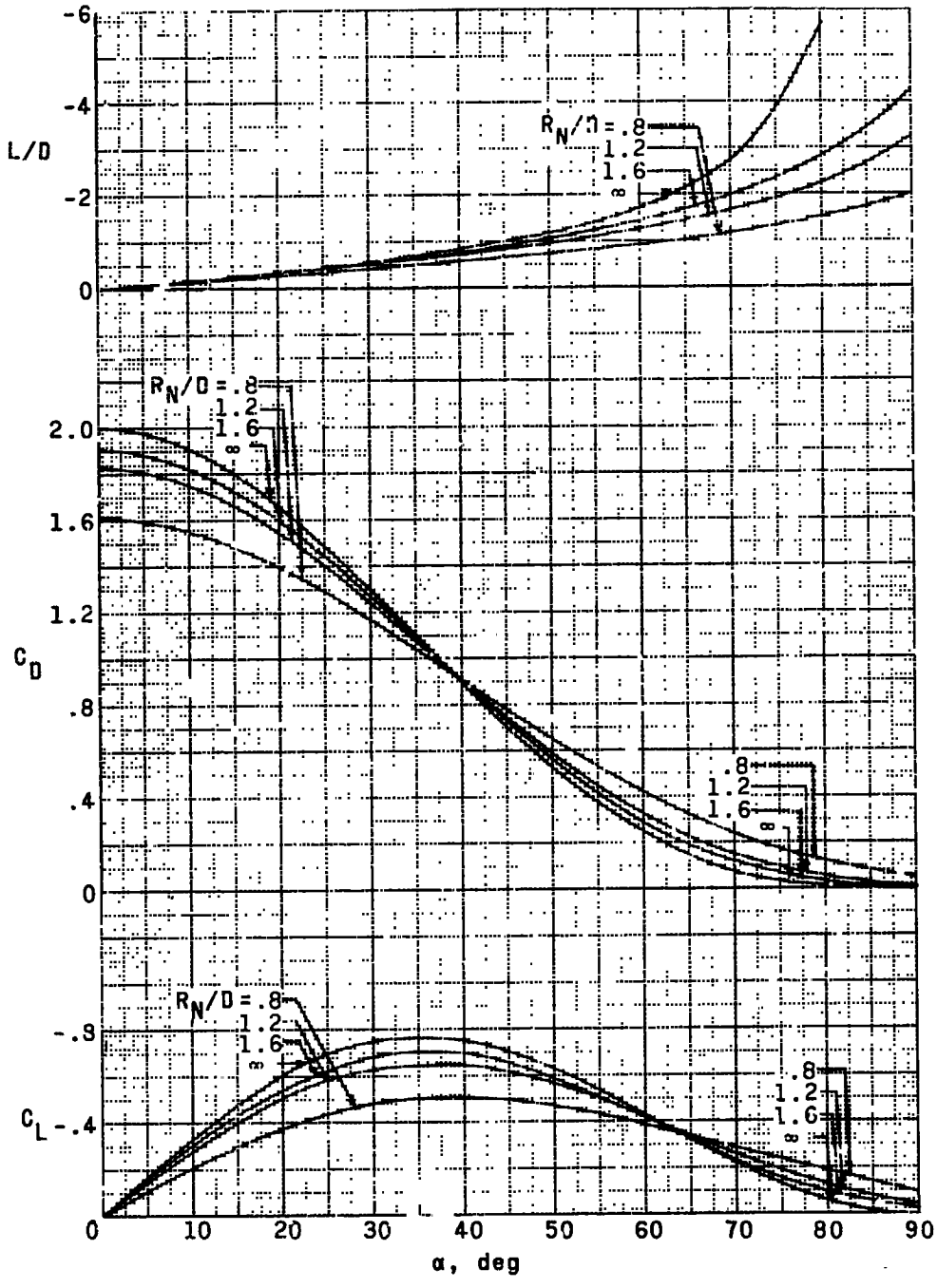

(a) Heat-shield contribution. (Concluded)

Figure 3.- Continued.

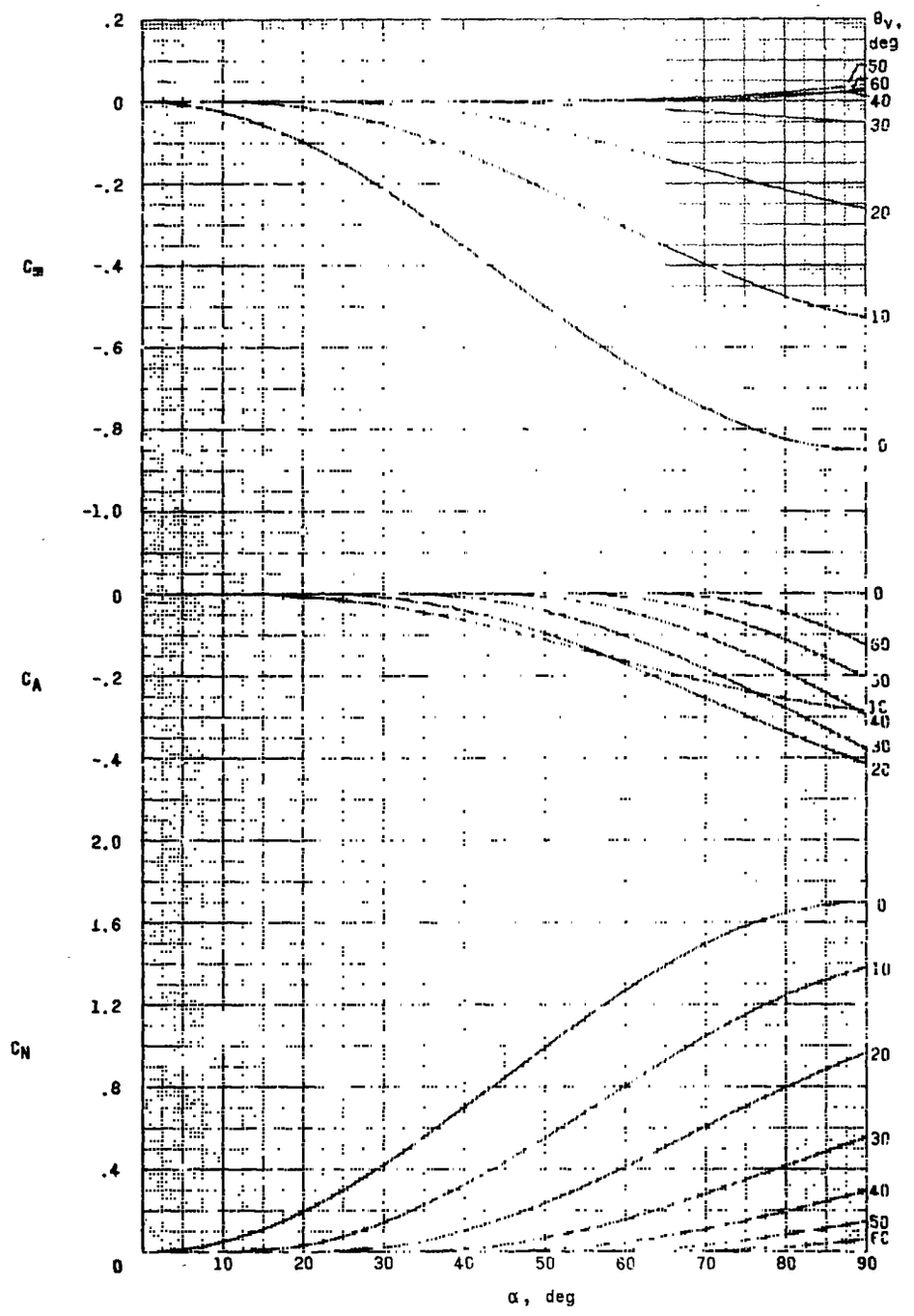

(b) Afterbody contribution.

Figure 3.- Continued.

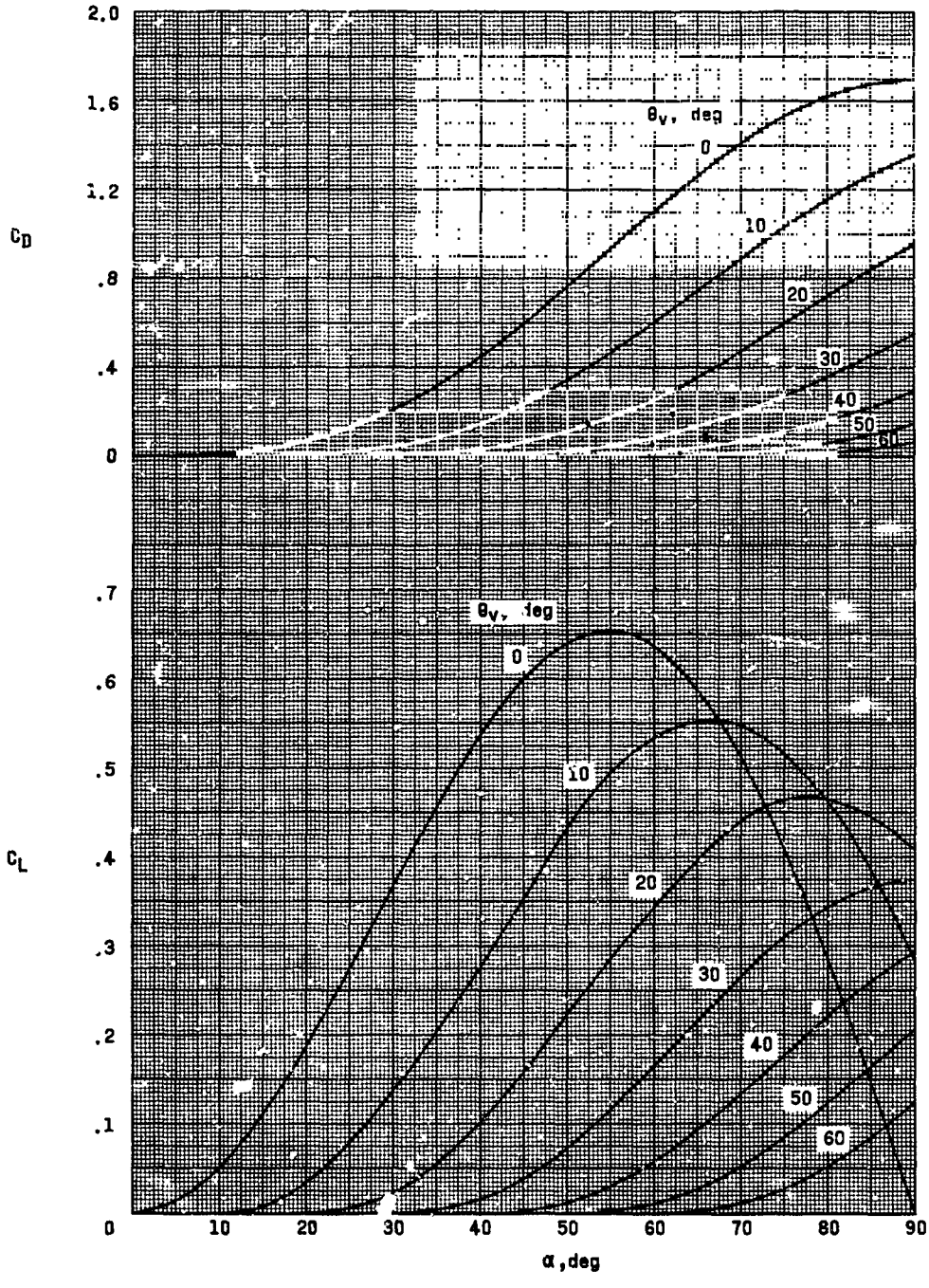

(b) Afterbody contribution. (Concluded)

Figure 3.- Continued.

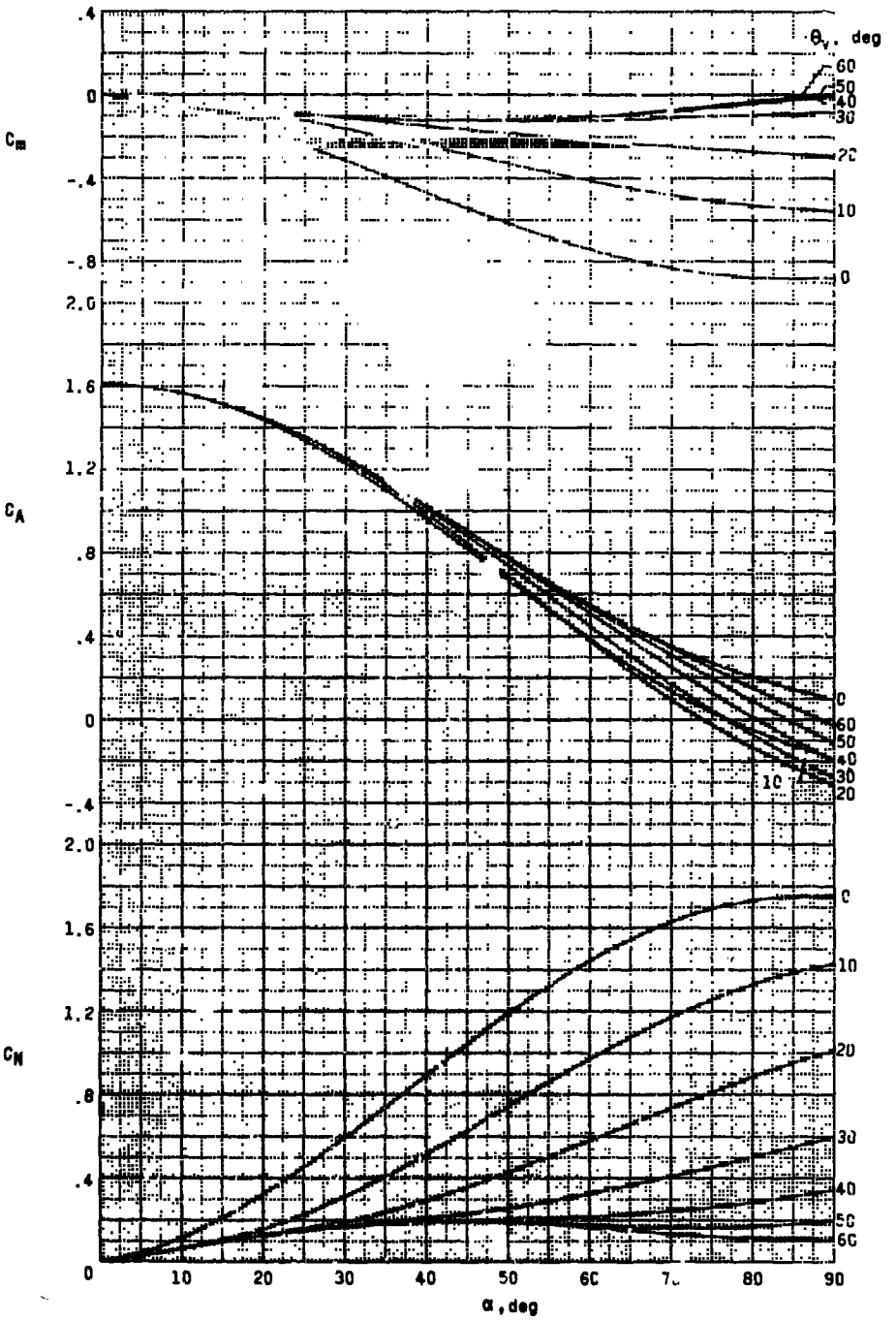

(c) Heat shield and afterbody combined. $R_N/D = 0.8$.

Figure 3.- Continued.

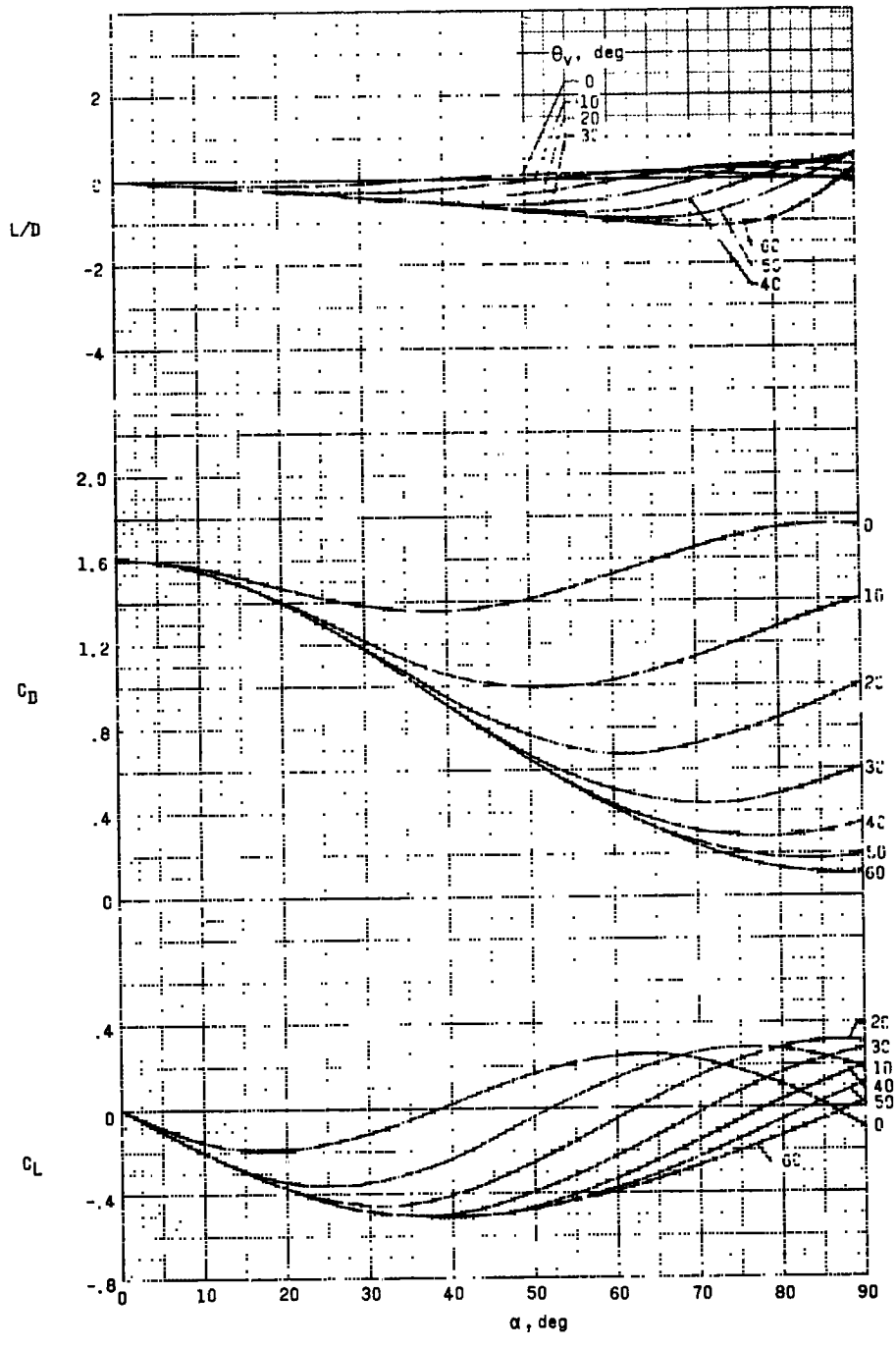

(c) Heat shield and afterbody combined. $R_N/D = 0.8$.

Figure 3.- Continued.

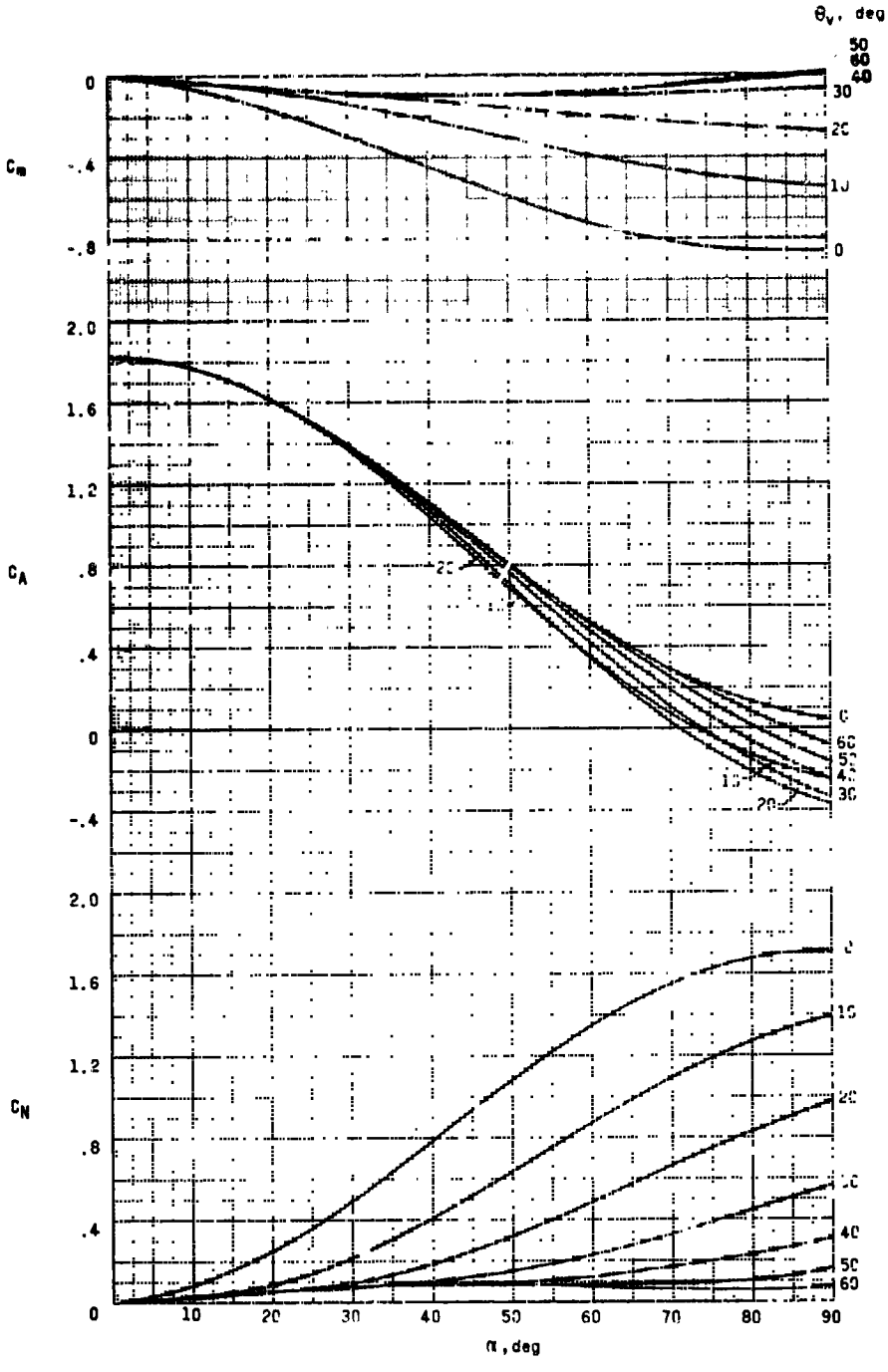

(c) Heat shield and afterbody combined. $R_N/D = 1.2$.

Figure 3.- Continued.

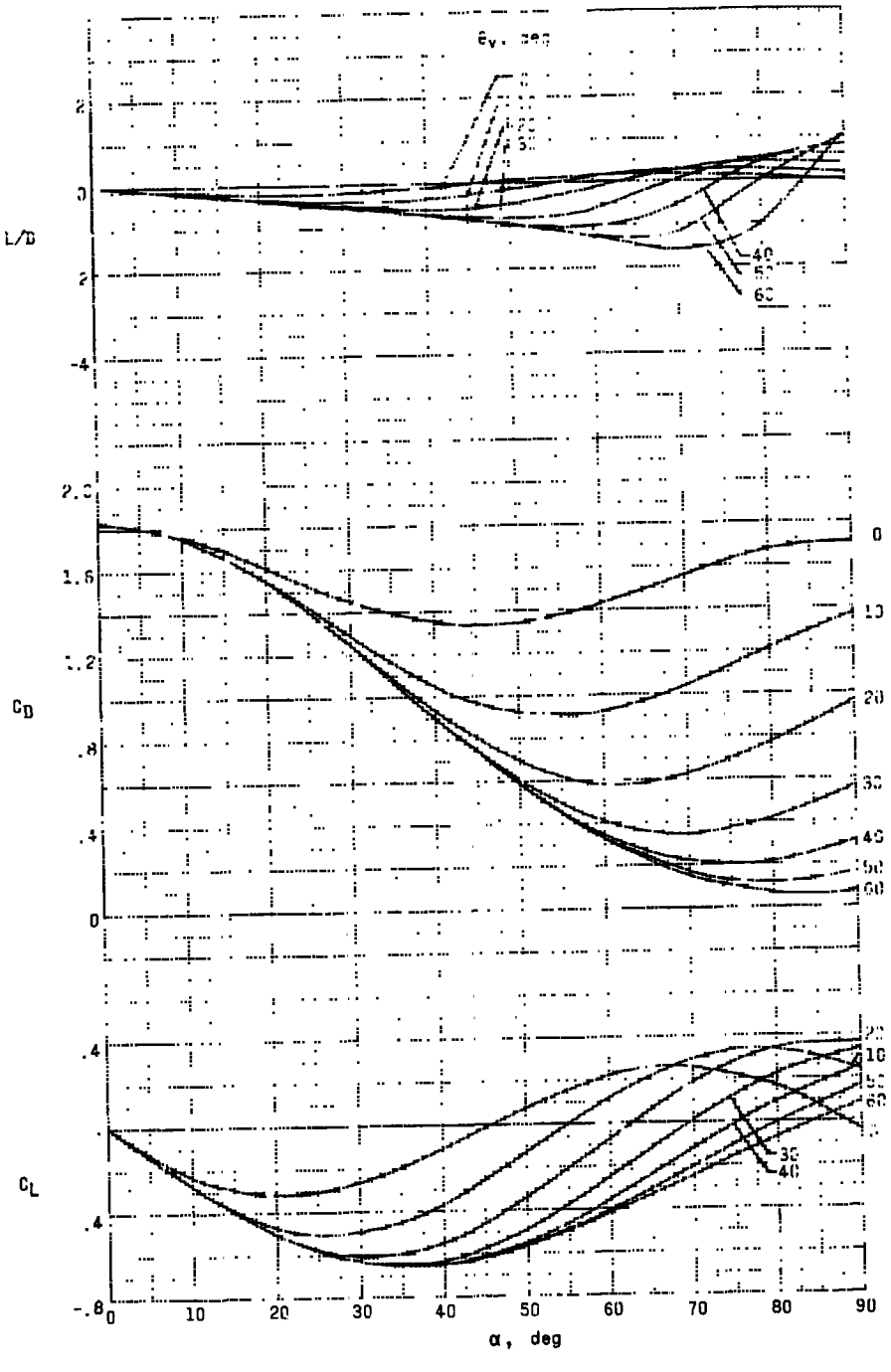

(c) Heat shield and afterbody combined. $R_N/D = 1.2$.

Figure 3.- Continued.

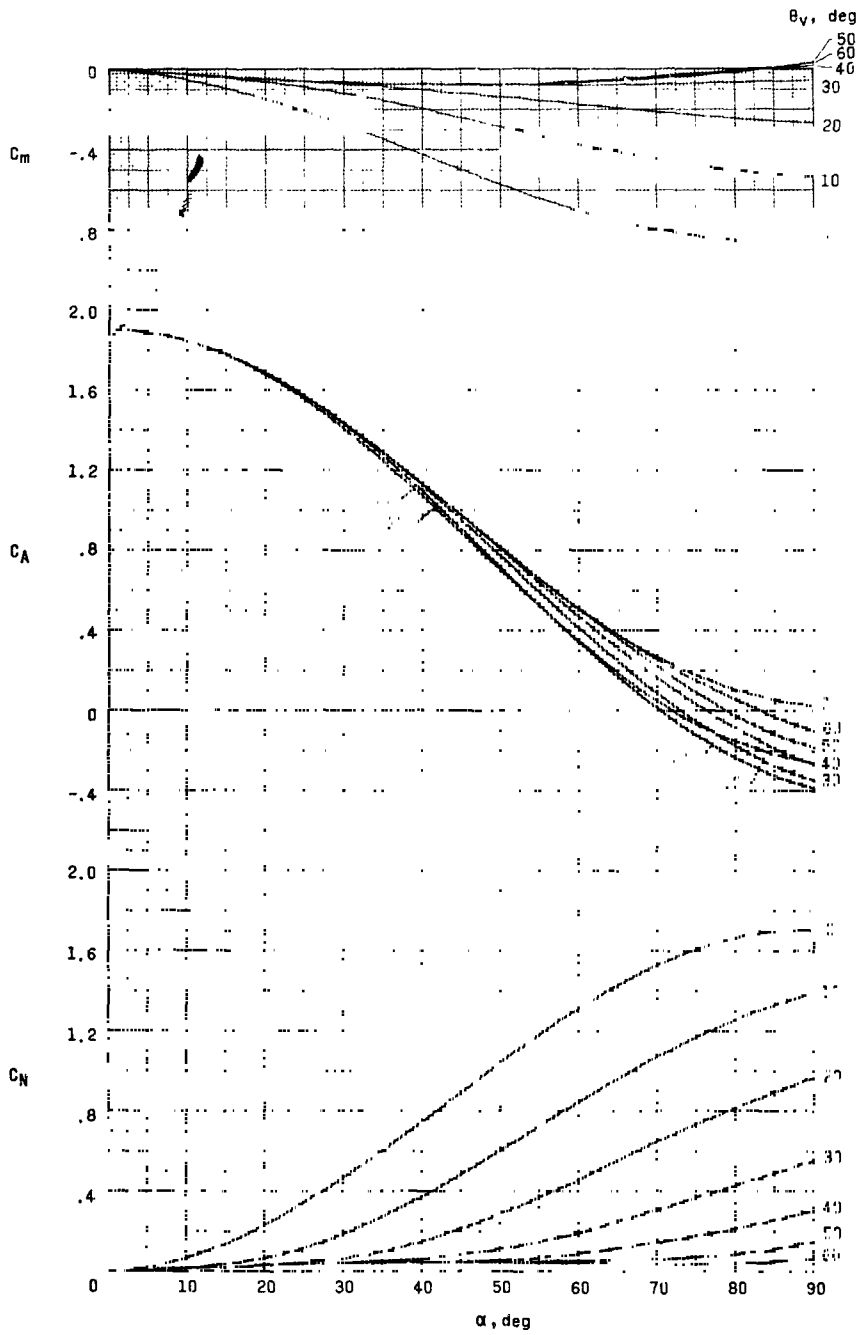

(c) Heat shield and afterbody combined. R_N/D = 1.6.

Figure 3.- Continued.

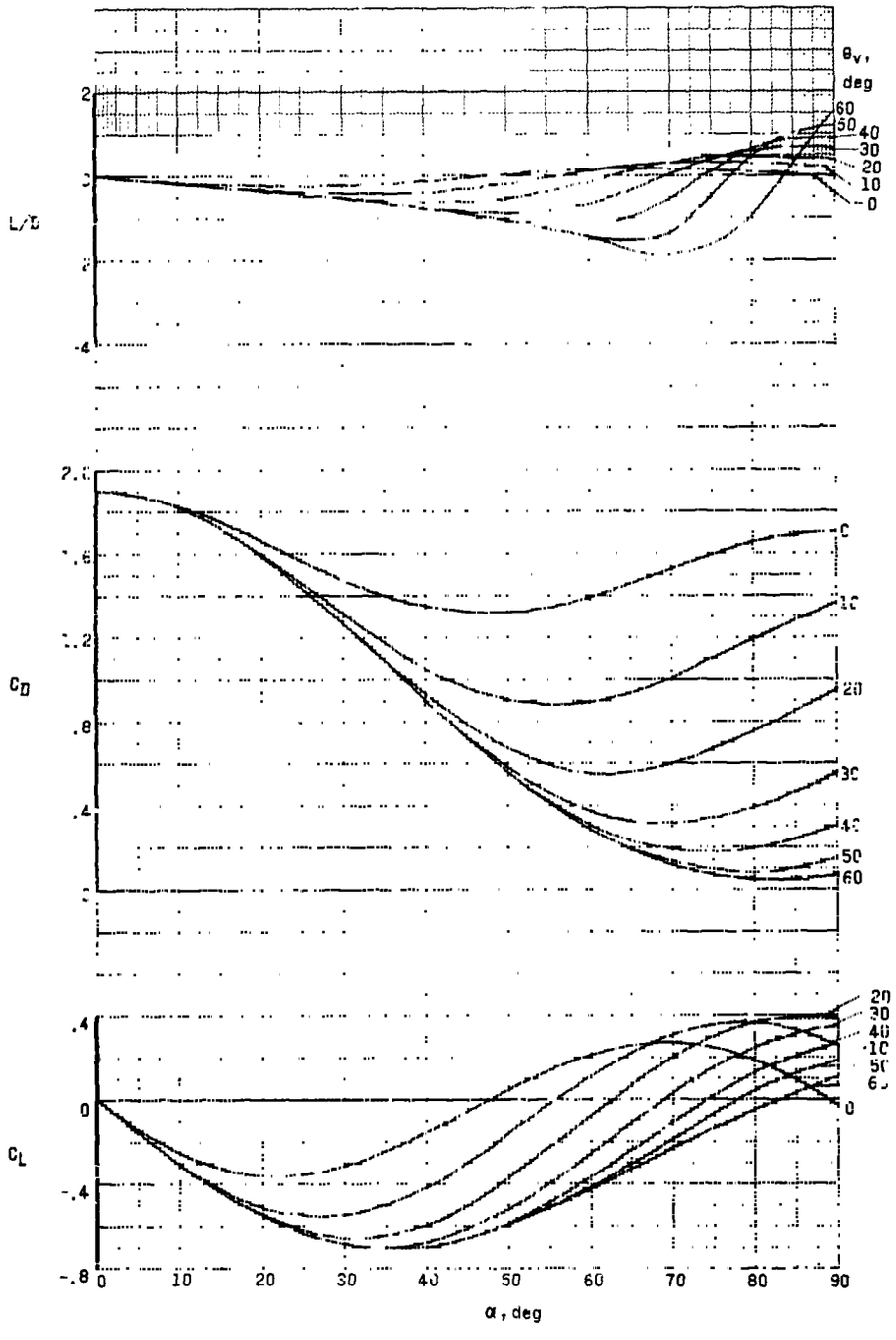

(c) Heat shield and afterbody combined. $R_N/D = 1.6$.

Figure 3.- Continued.

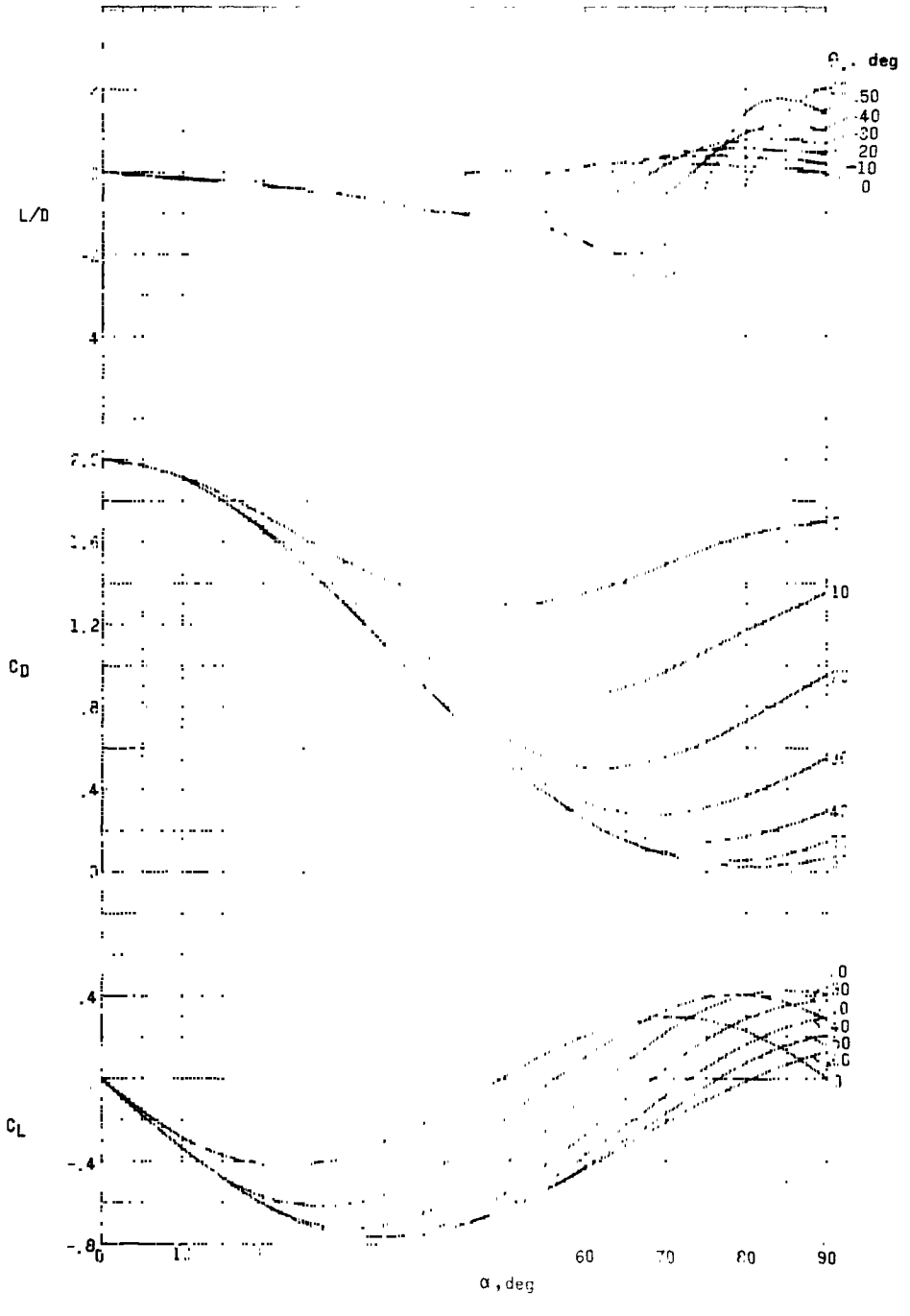

(c) Heat shield and afterbody combined. $R_N/D = \infty$.

Figure 5.- Continued.

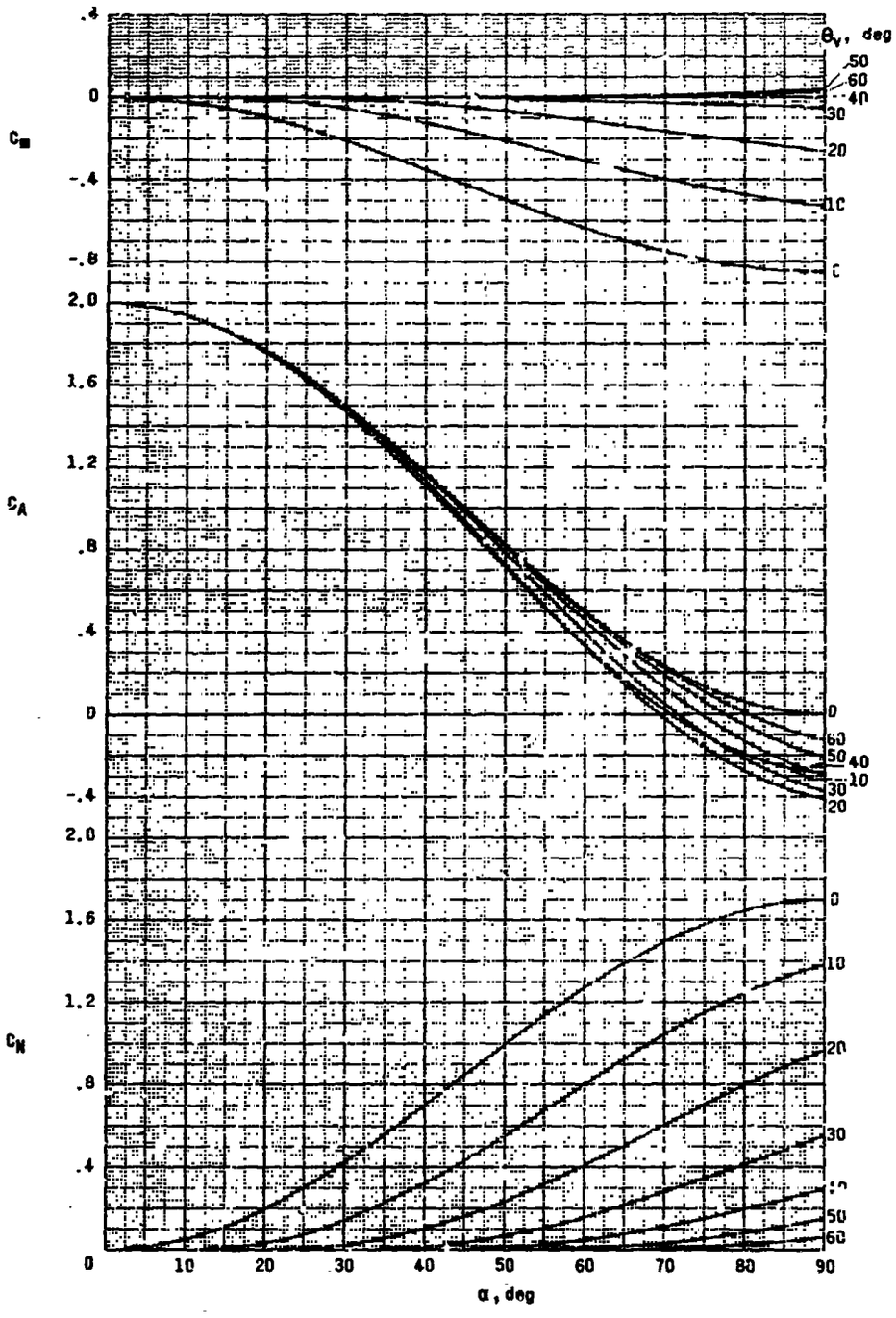

(c) Heat shield and afterbody combined. $R_N/D = \infty$. (Concluded)

Figure 3.- Concluded.

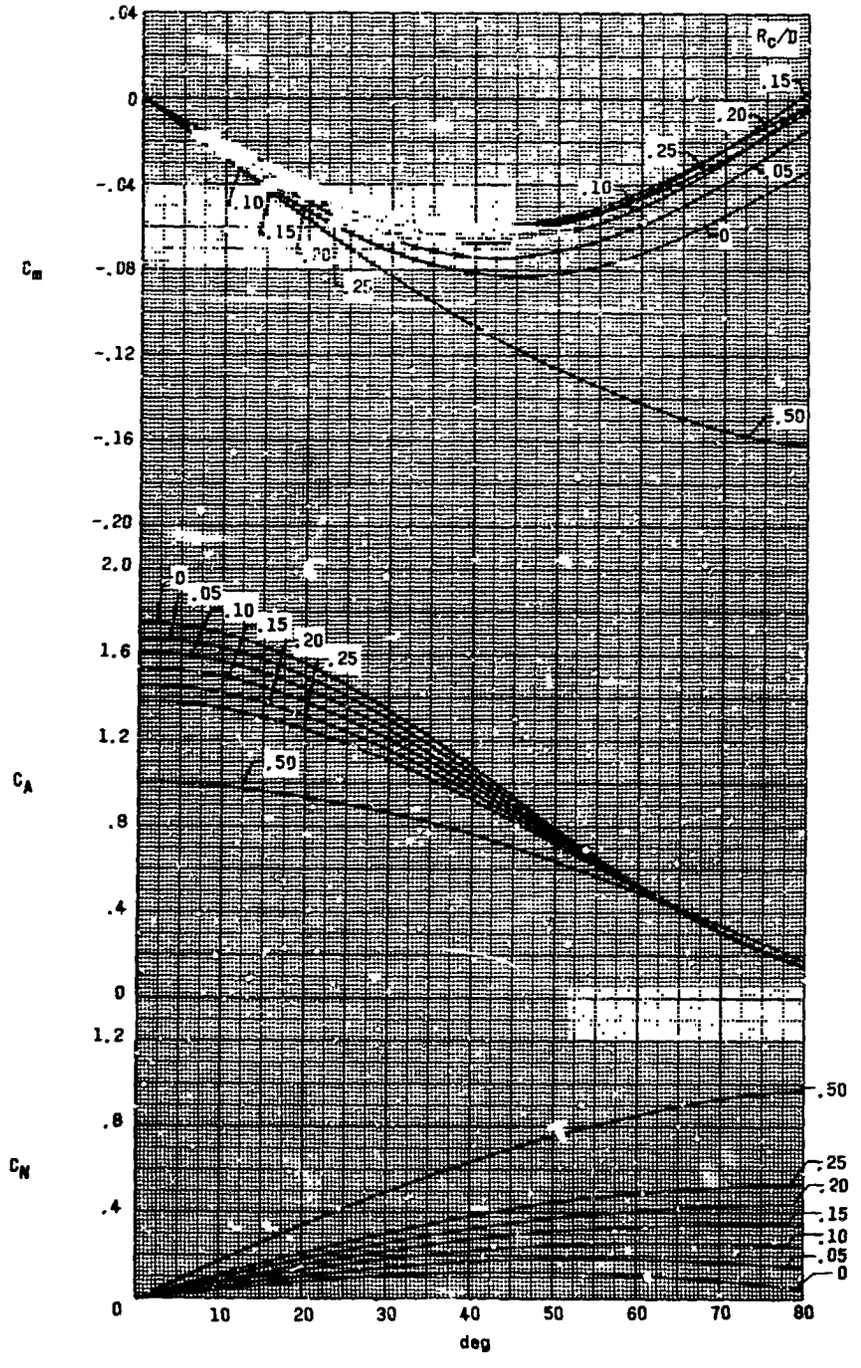

(a) $R_N/D = 1.0$.

Figure 4.- Corner-edge radius investigation.

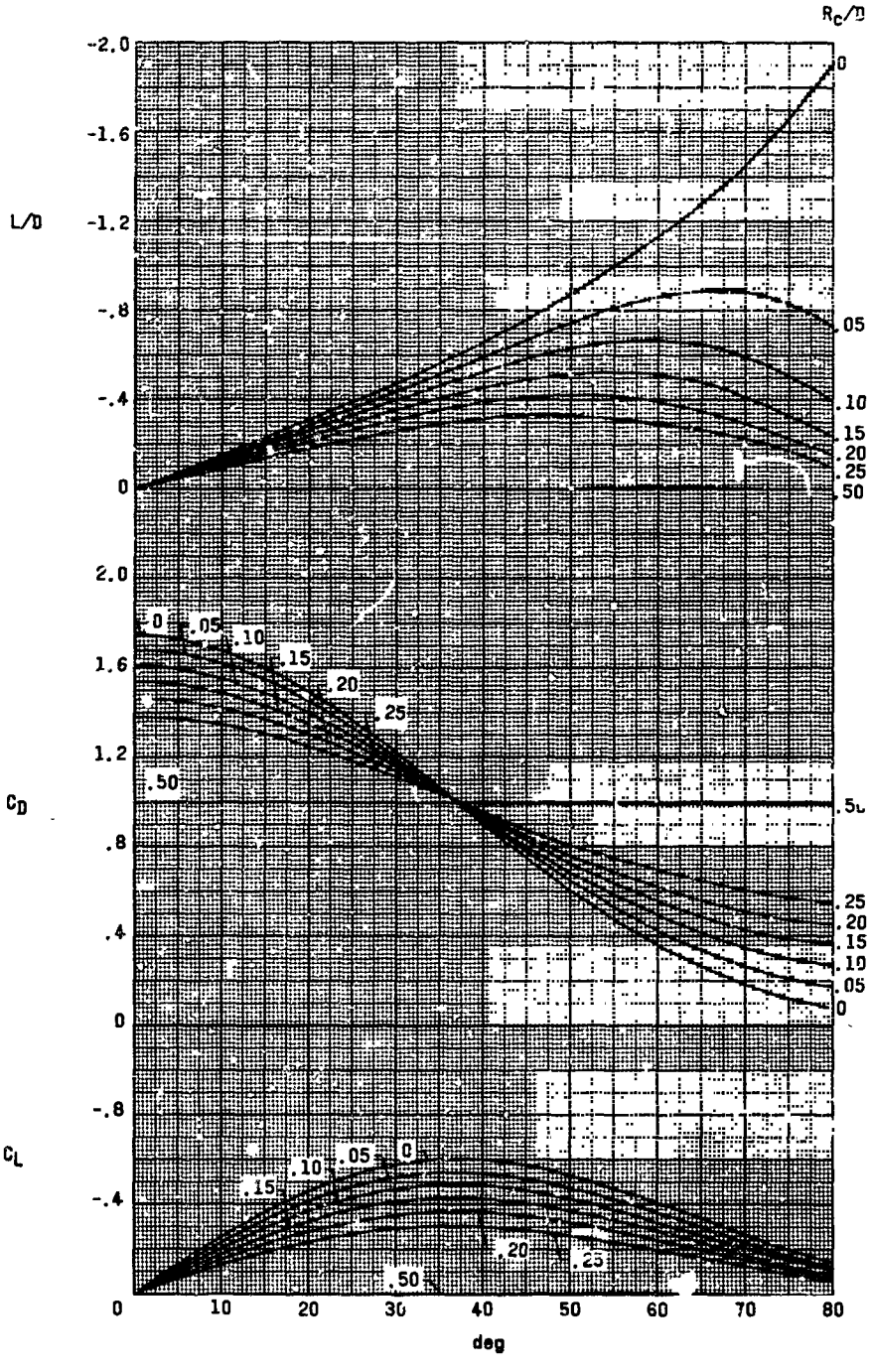

(a) $R_N/D = 1.0$.

Figure 4.- Continued.

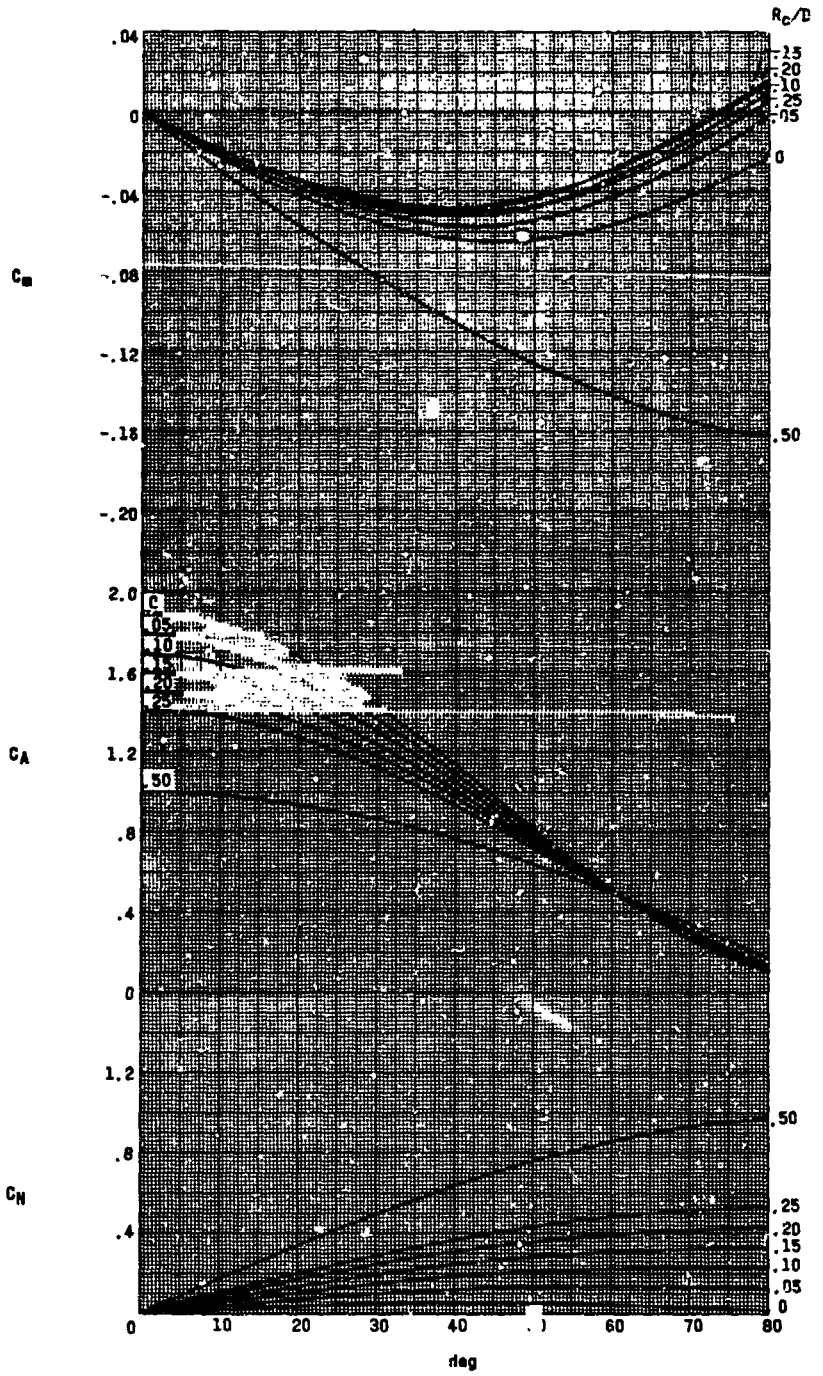

(b) $R_N/D = 1.5$.

Figure 4.- Continued.

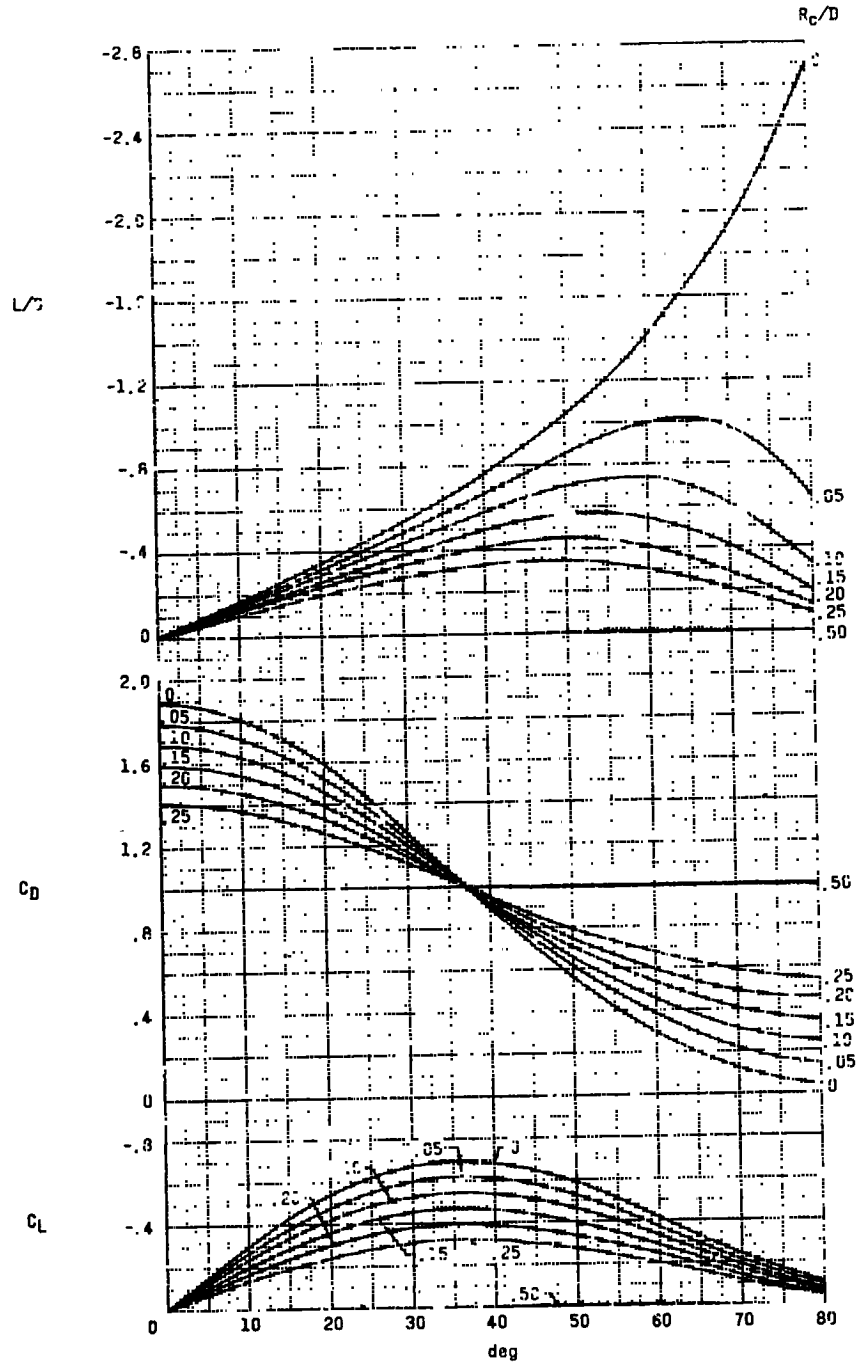

(b) $R_N/D = 1.5$.

Figure 4.- Concluded.

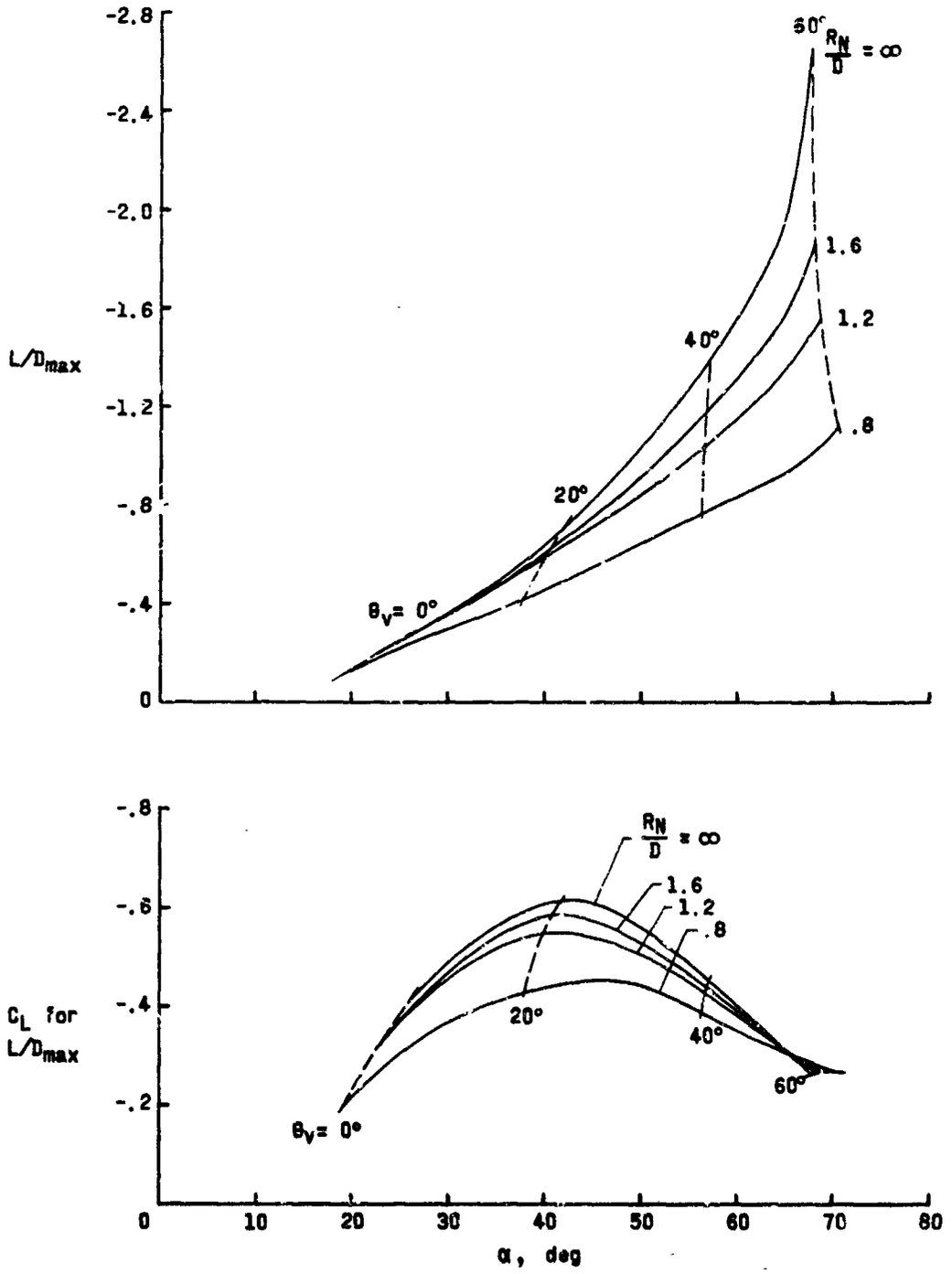

Figure 5.- Summary of combined heat shield and afterbody aerodynamic characteristics.

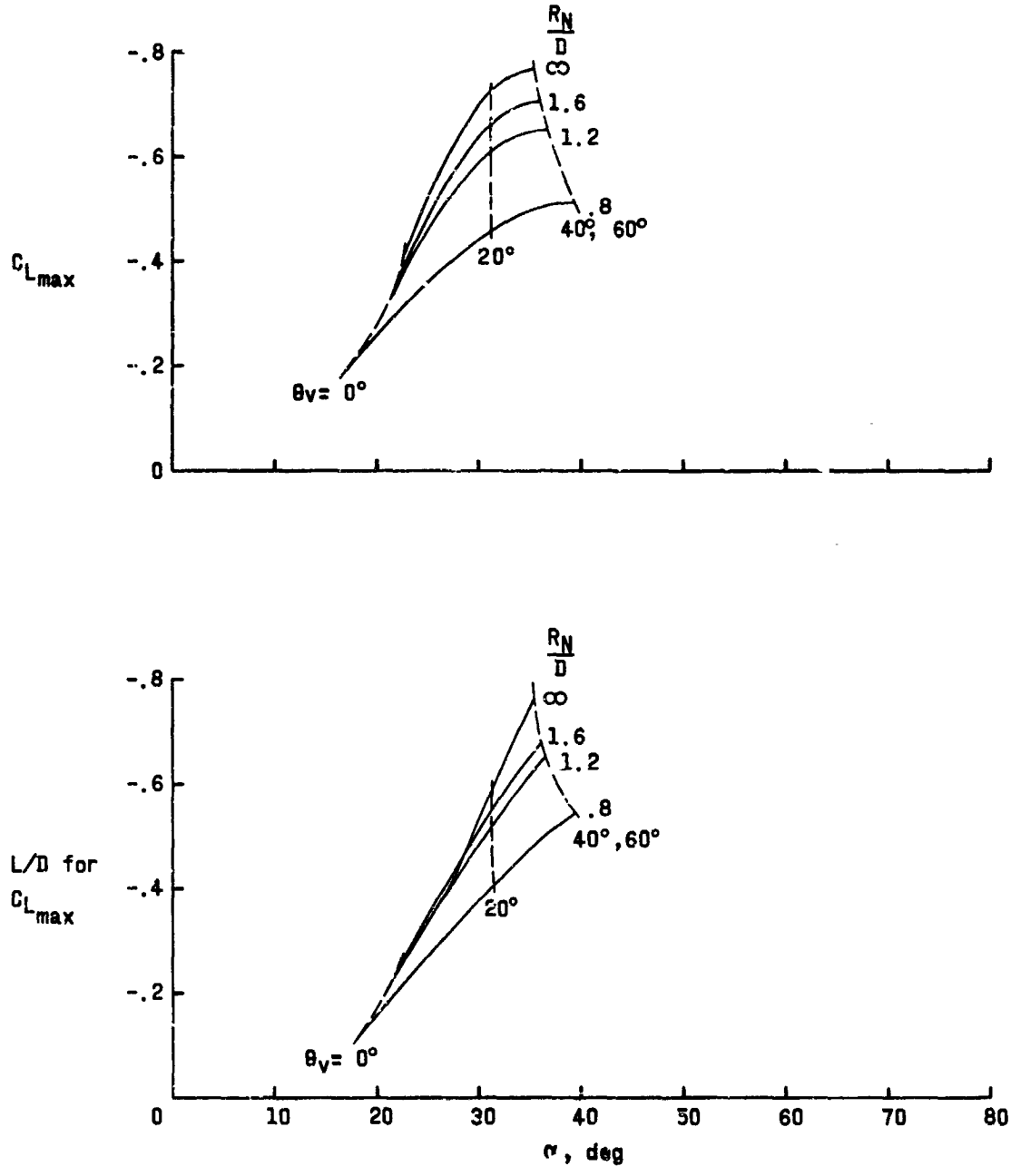

Figure 5.- Concluded.

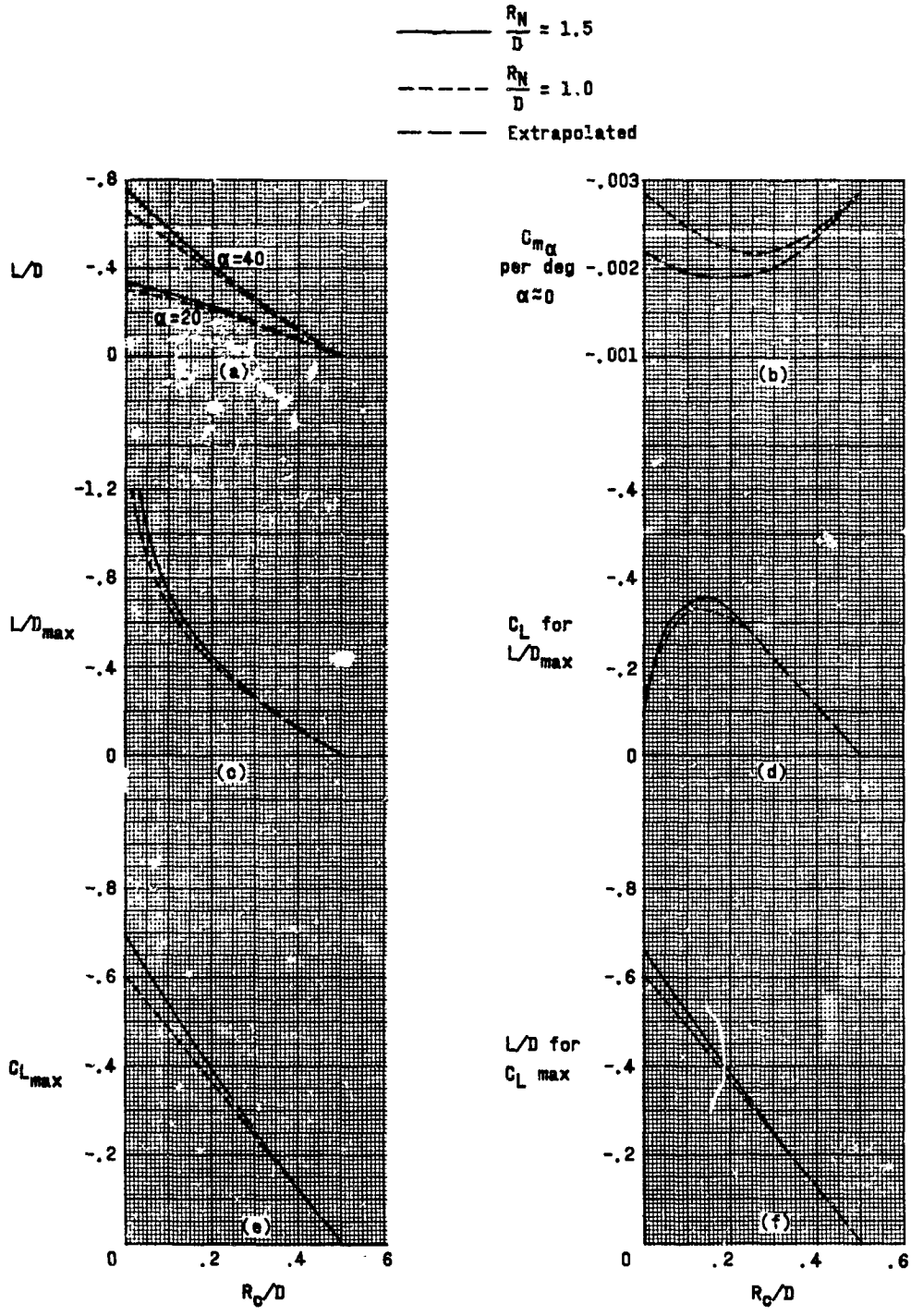

Figure 6.- Summary of corner-edge radius investigation.

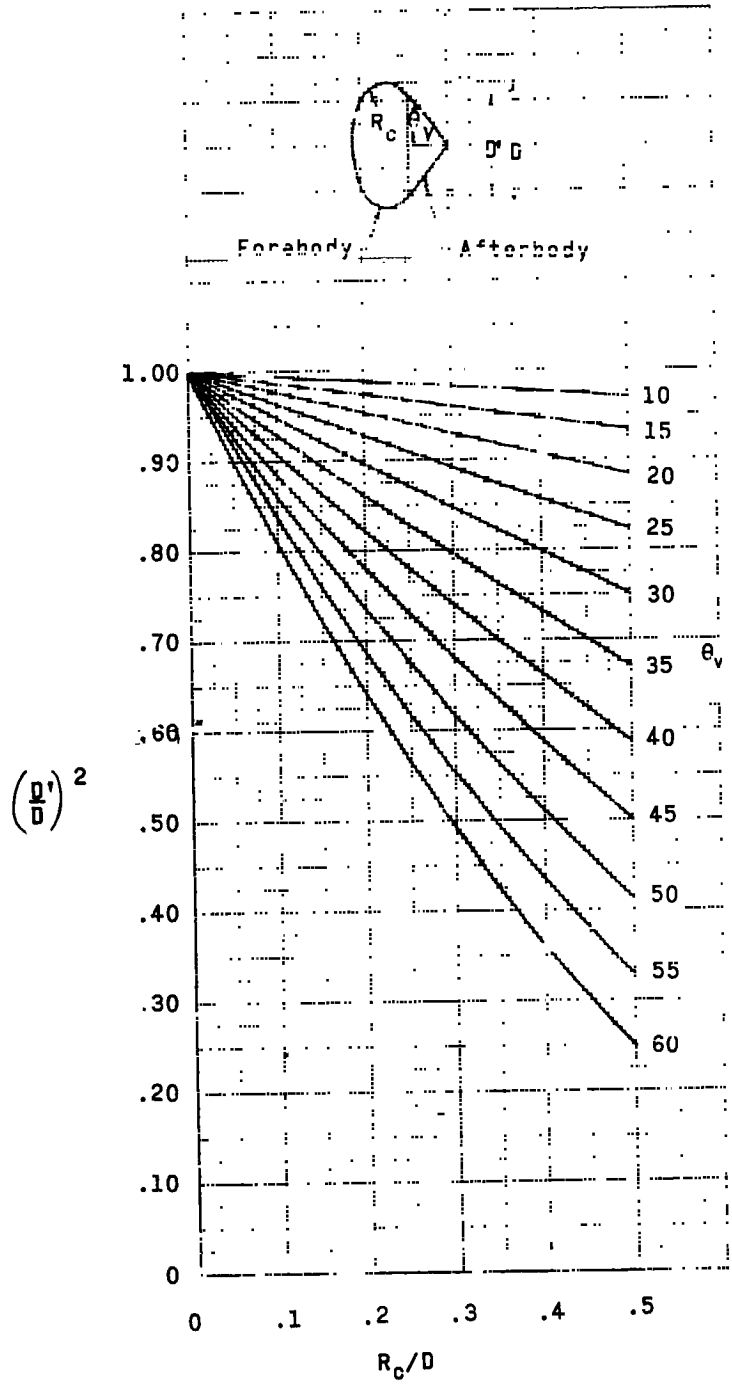

Figure 7.- Reference area ratio for combining corner-edge radius and afterbody contributions.

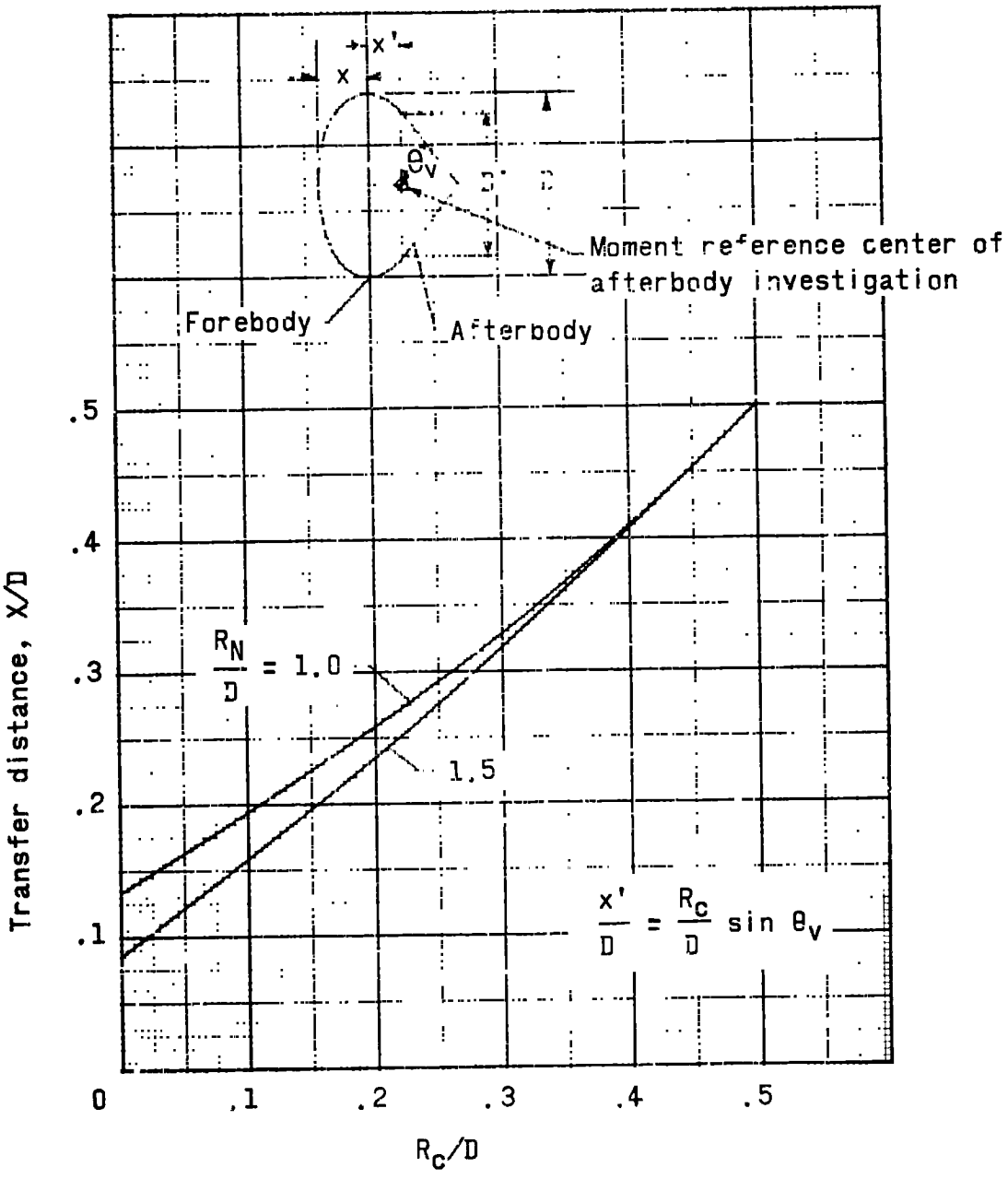

Figure 8.- Reference distances for combining afterbody and corner-edge radius moment contributions.

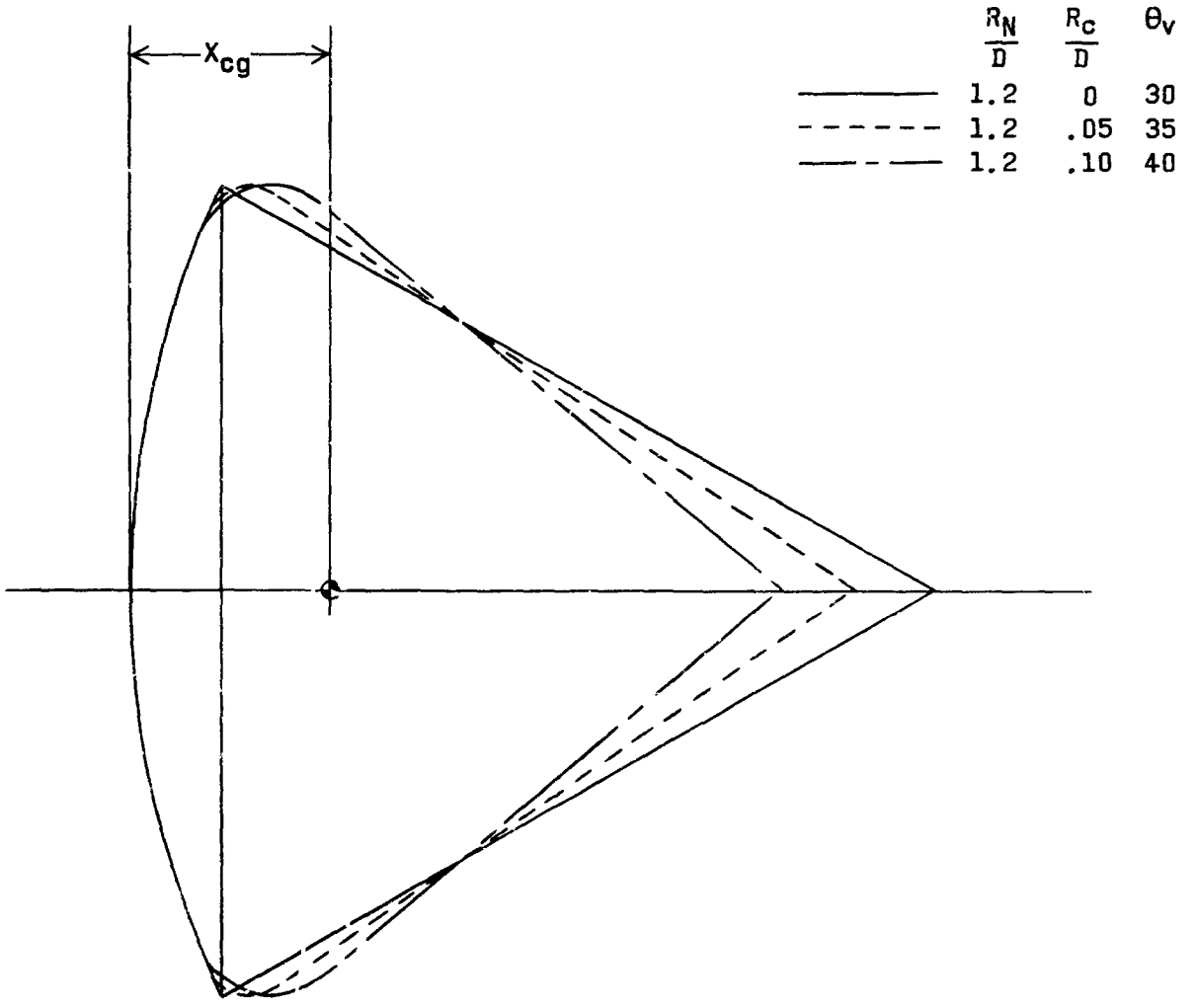

Figure A-1.- Geometric comparison of several configurations of equal volume.

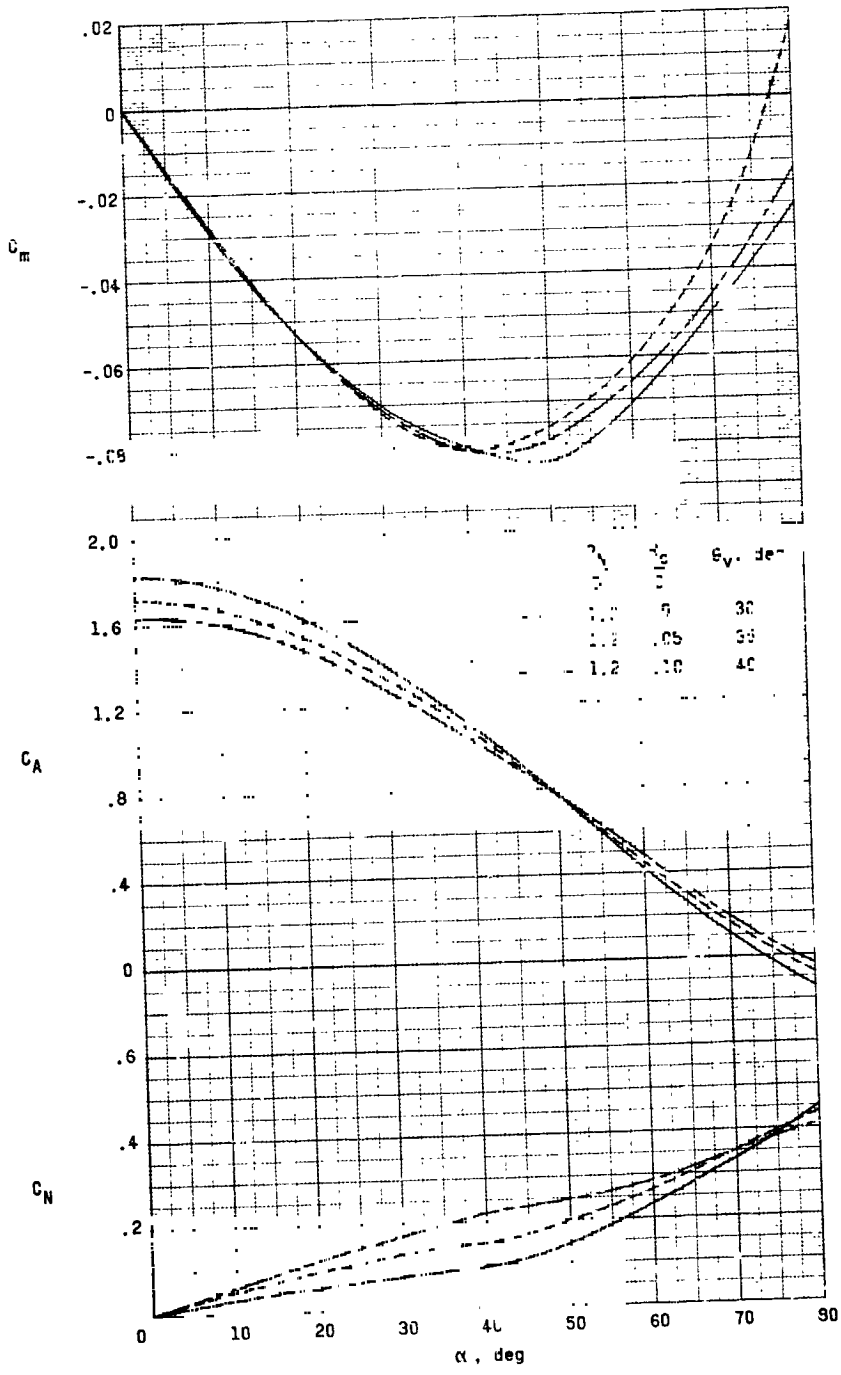

Figure A-2.- Comparison of aerodynamic characteristics for several configurations with equal volumes. $\frac{X_{c.g.}}{D} = 0.24$

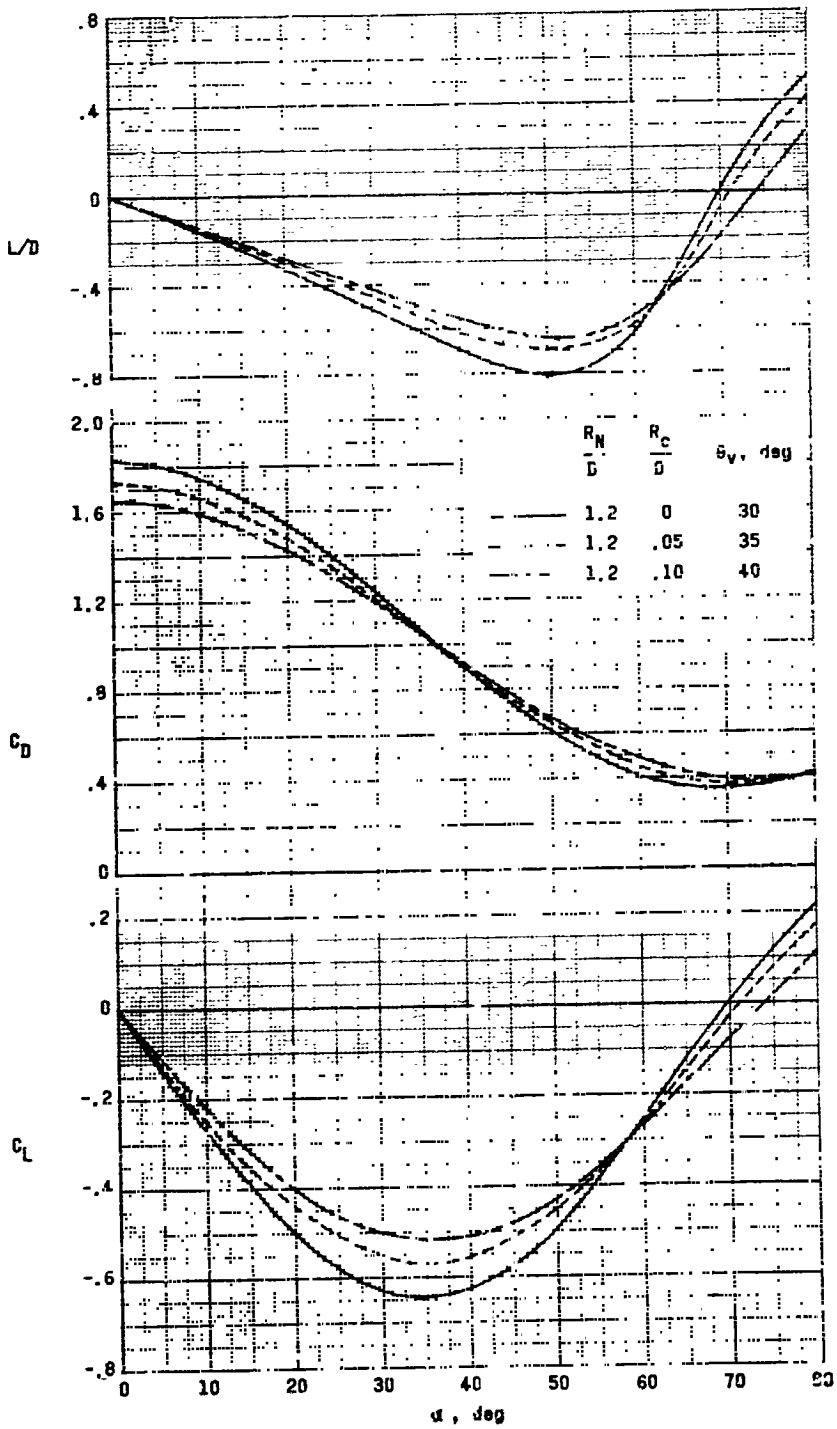

Figure A-2.- Concluded.

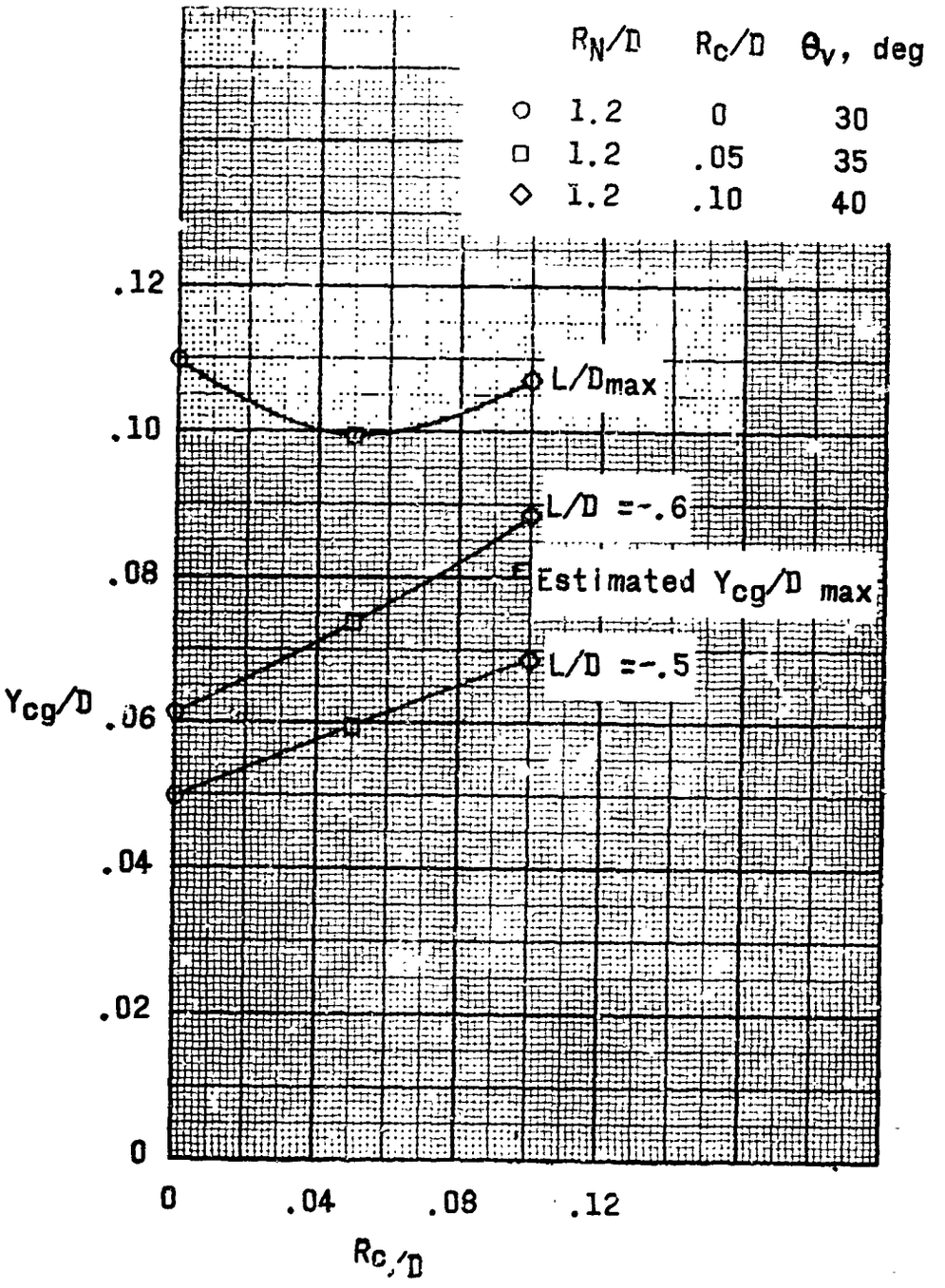

Figure A-3.- Lateral center-of-gravity offset required to trim at various lift-to-drag ratios for several configurations of equal volume. $\frac{X_{c.g.}}{D} = 0.24$